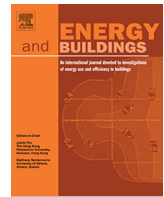




ELSEVIER

Contents lists available at ScienceDirect



Effect of an on/off HVAC control on indoor temperature distribution and cycle variability in a single-floor residential building

YiQin Xu, Yulia T. Peet *

School for Engineering of Matter, Transport and Energy, Arizona State University, Tempe, AZ 85287, USA

ARTICLE INFO

Article history:

Received 27 April 2021

Revised 29 June 2021

Accepted 15 July 2021

Available online 28 July 2021

Keywords:

On/off HVAC control

Cycle-to-cycle variability

Indoor temperature distribution

Computational fluid dynamics

ABSTRACT

This paper investigates an influence of an intermittent on/off operation of the air-conditioning (AC) equipment on the indoor temperature distribution, air flow and a cycle variability within a single-floor medium-size residential house. The analysis is performed using a recently developed and well validated computational tool based on a Computational Fluid Dynamics (CFD) method, coupled with conjugate heat transfer simulations within a three-dimensional model of a solid building envelope, and an HVAC on/off control model. The importance of including unsteady minute-level dynamic effects associated with the cycling of AC equipment into the energy and thermal analysis of residential and commercial buildings was recently recognized. Despite that, there were no studies that examined the effect of on/off cycling on the physics of the air mixing during both cooling and heating stages of the AC cycle, and how these unsteady interactions effect both the energy consumption and its variability, and the indoor thermal environment linked to a thermal comfort of the building occupants. The current paper focuses on analyzing the duration and variability of the cooling and heating cycles and their effect on the temperature distribution inside a residential house. It is found that both heat transfer from the walls, and turbulent intermittency of the indoor air affect the duration of the cooling and heating cycles. It is demonstrated that a central air system controlled by a single thermostat placed in the hallway results in a consistent overcooling of the interior spaces. These findings are important for the considerations of the electric grid management, and for the improvement of HVAC systems design and control.

© 2021 Elsevier B.V. All rights reserved.

1. Introduction

Heating, ventilation and air-conditioning (HVAC) systems represent an important component of a building infrastructure. Consequently, there were many studies concerning the effect of HVAC system on building energetics [1,2] and indoor thermal comfort [3,4]. However, most of these studies considered a continuous operation of HVAC systems, where equipment was assumed to run constantly. However, in reality, HVAC units do not deliver a constant supply of air, but, depending on the control system, either adjust the airflow dynamically, or simply cycle on and off. The dynamic effects of the HVAC system operation are important considerations with regards to their performance, and represent the main focus of the current paper.

HVAC control system is responsible for adjusting the equipment operation, so that the temperature is maintained within the narrow band (a “deadband”) around a desired temperature, which is typically set by the thermostat setpoint [5,6]. Most of the HVAC

units currently installed in the residential single-family homes in US and worldwide rely on a simple on/off switch to control the temperature [6–8]. During an on/off temperature control, for example, for an air-conditioning (AC) mode, the unit operates at 100% capacity when the temperature is above the upper bound of the deadband, it turns off when the temperature reaches the lower bound of the deadband, and turns on again when the temperature exceeds the upper bound [5,9,10]. The time intervals during which the equipment is running or turned off, depends on many factors, including the outdoor temperature, the thermal characteristics of the building envelope, the size of the indoor space served by the unit, and the capacity of the unit [10–12]. For example, it was noted that oversized units, facing part-load operating conditions, result in shorter cycles and, thus, more frequent on/off switches during the system operation [13,14]. According to recent reviews, most of the units installed in the residential houses are oversized, i.e., they meet their design conditions only less than 2% of the time, and operate in a part-time load for 98% of their functional use [15,16].

Part-load and cyclic operation of the HVAC units are important considerations that effect a variety of aspects associated with the

* Corresponding author.

E-mail address: yipeet@asu.edu (Y.T. Peet).

performance and functionality of an indoor thermal management system, such as energy efficiency [13,17], sensible and latent heat exchange capacity [18,19], load variability [20,21], and thermal comfort [12,22]. Henderson et al. [23] and Booten et al. [24] used building energy simulation tools to investigate the effect of part-load operation on energy efficiency and found that it is reduced. Henderson et al. [18] introduced a new user defined function into a DOE-2 simulation tool to account for a change in sensible and latent capacity with part-load conditions and investigated the effect on moisture removal efficiency. Cetin et al. [10] implemented a real-time on/off cycling control model into EnergyPlus and compared it with the field data for a residential house. They found that an inclusion of an/off control model improved the accuracy of prediction by as much as 20% for both the cooling power and the indoor air parameters (temperature and humidity). Surprisingly, both the field data and the EnergyPlus simulations data not only reveals the presence of the indoor temperature fluctuations during the AC equipment cycling, but also shows that the duration of the AC cycles themselves varies substantially from cycle to cycle. This cycle-to-cycle variability further contributes to uncertainties in a power demand and electric grid fluctuations [21,25,26], and might effect the temperature distribution inside the house and lead to an increased discomfort for its occupants. Additionally, it needs to be accounted for in the corresponding reduced-order models [10,18]. As such, the source of this variability needs to be understood, and potential mitigation strategies need to be identified, which is the goal of the current paper. Note that similar cycle-to-cycle variability was previously observed in other thermo-fluid problems, for example, during internal combustion engine operation [27,28], and it seems to be associated with a dynamic behavior of thermal turbulent structures under quasi-periodic conditions. Since study of Cetin et al. [10] was performed using a building energy simulation tool that uses zonal models, which are unable to resolve the interior turbulent structures, the authors of Ref. [10] could not investigate the origin of cycle variability in detail, which prompts the current study of the phenomenon using Large Eddy Simulations.

The objective of the current paper is to investigate the effects of the on/off operation of the AC equipment on the indoor airflow and temperature distribution inside a residential multi-room single-floor building using a high-resolution Computational Fluid Dynamics (CFD) approach. Such information is of high demand for the building industry and thermal system design sector, and it serves two purposes. First, it allows one to evaluate the level of thermal comfort of the occupants in the presence of the cyclic AC operation. For example, Ulpiani et al. [12] compared the effect of different thermostat control strategies on the energy consumption and indoor thermal comfort using an experimental single-room mock-up building model and concluded than an on/off HVAC controller resulted in the lowest comfort level. The current study provides a guidance on why an on/off AC control could result in a low thermal comfort level, and also makes suggestions about the measures that could be taken to improve the thermal comfort of the occupants. Second, the current study documents the role of an air turbulence on the duration and variability of the cooling and heating parts of the HVAC cycles. This information is crucial for understanding the equipment cycling effects on operation and stability of electric grid networks, such as, for example, in regards to a demand response management, stability of the power supply, and electric grid frequency regulation [21,25,26]. In addition, the collected high-fidelity database can be used for validation and improvement of lower-fidelity building simulation tools in the presence of an on/off AC cycling.

CFD techniques have been previously applied quite successfully to analysis of a thermal comfort and ventilation systems performance both inside small spaces, such as offices [29–31] and rooms

[32–34], and also larger spaces, such as a theater building [35], and an auto-racing complex [36]. These studies, however, were mostly focused on analysis of performance of the radiator systems [31,34], fan-coiled heating systems [30], natural ventilation environment [29], and a cooking fume distribution in a kitchen environment [33], rather than performance of the AC cooling systems. Shan et al. [32] investigated a thermal environment in an office room with a fan-coil cooling unit, Nada et al. [35] compared a performance of an underfloor air distribution system and a traditional overhead mixing air distribution system for a theater building, while Chen et al. [37] investigated the effect of air-supply speed and temperature on the performance of an air-conditioning system in a ventilated cooling room. However, these studies did not consider two important aspects associated with realistic HVAC operation in a building environment: 1) the effects of unsteady operation of HVAC equipment, and 2) the effects of the heat transfer between the interior air and the building walls.

Regarding the problem of heat transfer between the air and the building walls, it was shown to be beneficial to couple CFD models with the building energy simulation tools to obtain the information regarding realistic wall surface temperature and heating/cooling loads [36,38–41]. However, building energy simulation tools, even when used only for the solid parts of the building, still can not provide a proper resolution of spatial and temporal scales associated with unsteady heat exchange between the solid building components and an interior turbulent air. To represent unsteady thermal phenomena on the time scales that interact with the turbulent thermal convection, a framework of a conjugate heat transfer (CHT) is useful, wherein an unsteady heat conduction equation is solved inside a corresponding three-dimensional model of the building envelope, concurrently, and using a compatible spatial and temporal resolution, as the fluid dynamics CFD equations. Being a high-fidelity modeling technique, CHT was previously applied mostly to canonical studies of natural convection in isolated enclosures [42–44], thermal environment in small room configurations [45,46], or analysis of thermal performance of building blocks with cavities [47–49], radiant cooling panels [50,51], and heat exchangers [52,53]. In the current study, we apply the CHT simulation to investigate performance of an on/off HVAC operating unit in a medium-size multi-room residential house. As shown in the previous studies, CHT allows for an accurate prediction of a coupled dynamics of an airflow and a heat transfer between the fluid and the solid. To the author's knowledge, an application of a conjugate heat transfer model to study a performance of an air-conditioning system within a multi-room medium-scale residential house with a dynamic HVAC operation has not previously appeared in the literature.

The current study considers a medium-size building typical of a single-family home in Arizona, using the operational conditions relevant for a summer day in a Phoenix climate. We use a well-validated open-source spectral-element fluid dynamics and heat transfer solver Nek5000 [54] for CHT simulations, while a turbulent air flow is modeled using a Large Eddy Simulation technique [55,56]. Large Eddy Simulation provides a more accurate model for the computation of turbulent motions, important in the current study of AC cooling jet dynamics, mixing and heat transfer, but requires a finer computational grid and smaller time steps compared to traditional Reynolds-Averaged Navier–Stokes equation models. The paper is organized as follows. In Section 2, we present the numerical methodology, the building model, geometry and the simulation strategy; Section 3 documents a detailed validation of the presented computational tool; Section 4 presents the results of the implemented case study, including 1) duration and variability of the cooling and heating parts of the consecutive HVAC cycles, 2) comparison between a thermostat sensor temperature and the averaged room temperatures, 3) airflow and temperature distribu-

tion in the rooms during the cooling and switch-off (natural heating) HVAC operation. Section 5 draws conclusions.

2. Modeling methodology

2.1. House model

A housing model in this study is taken as a 755.11 square feet residential home with four rooms, featuring two bedrooms, an open-floor living area that includes the kitchen, and a long hallway dividing the bedrooms and the living area. The house floor plan is presented in Figs. 1, 2, where green color represents the house interior, gray is the building envelope, black color represents the door, and blue color corresponds to the windows. Room 1 and Room 2, the bedrooms, have the same area of $4 \text{ m} \times 3.6 \text{ m}$ (155 square feet), albeit Room 2 has a window ($0.8 \text{ m} \times 1.2 \text{ m}$) for testing the glazing effect, which can be seen in a three-dimensional view in Fig. 3(a). The bottom edge of the window is located 1 m above the ground, and its closest vertical edge is 0.4 m away from the partition between the Rooms 1 and 2. The ceiling height of the house is 2.6 m. Room 1 and Room 2 both have an air supply vent ($0.2 \text{ m} \times 0.2 \text{ m}$) in the ceiling located 1.4 m away from both interior partitions in each room (with Room 3 and between the Rooms 1 and 2), which can be viewed in Fig. 4.

Room 3 ($1.2 \text{ m} \times 7.4 \text{ m}$) represents a hallway, and it does not have an air supply vent, but has an air return vent ($0.4 \text{ m} \times 0.6 \text{ m}$) located at the ceiling in the center of Room 3 as can be seen in Fig. 4(a). Room 3 also includes a front door ($0.8 \text{ m} \times 1 \text{ m}$) colored in black, please, refer to Figs. 1 and 3.

Room 4 is considered as a living space with an area of $4 \text{ m} \times 7.4 \text{ m}$, and it includes two ceiling air supply vents, both of $0.2 \text{ m} \times 0.2 \text{ m}$, located 2 m away from the partition between the Rooms 3 and 4, and from each side of the building envelope. Room 4 also comes with two glass windows colored in blue, one for the kitchen ($1 \text{ m} \times 1.2 \text{ m}$), and another for the balcony ($1.8 \text{ m} \times 2.4 \text{ m}$), which can be viewed in Figs. 1 and 3(b). The kitchen window's bottom edge is 1 m away from the ground, and the closest vertical edge is 0.8 m away from the building envelope. The balcony window extends all the way down to the ground, and has its closest vertical edge 2.8 m away from the envelope.

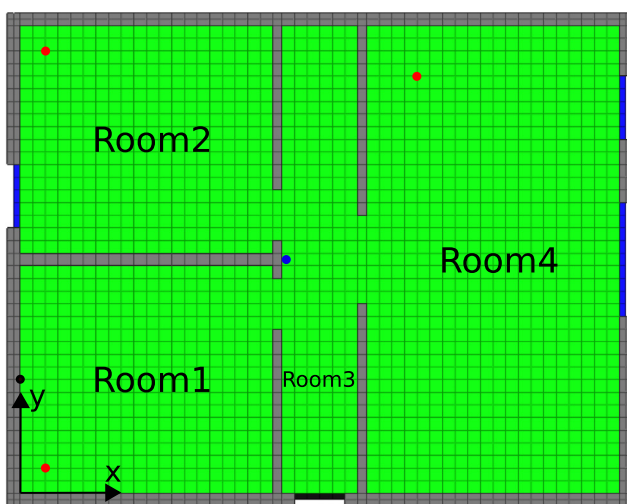


Fig. 1. Floor plan and the building envelope at a height of 1.6 m. Blue dot corresponds to a thermostat probe; red dots, remote temperature probes within the rooms; black dot, a wall temperature probe for the initial heating stage of the simulations.

The partition walls adjacent to Room 3 are 0.14 m thick, and the partition between Rooms 1 and 2 is 0.2 m thick. The inner wall of the building envelope is 0.1 m thick, except for the inner roof wall, which is 0.2 m thick. The outer wall and the outer roof are both 0.1 m thick, as can be seen in Fig. 2. The total housing area is 70.152 m^2 (755.11 square feet) including the partitions. The house is modeled after a two-bedroom residential condo plan of the IMT Desert Palm Village in Tempe, AZ.

2.2. Material properties

There are three types of materials used to model the building envelope: Douglas Fir wood for the exterior walls, exterior roof and the door; LD-C-50 spray foam for the insulation; and glass for the windows. Insulation is used in all the inner walls, including the inner parts of the building envelope, inner roof, and the interior partitions between the rooms. The material parameters used in the current study are listed in Table 1. The interior part of the house shown in green in Fig. 1, Fig. 2 is considered to be occupied by an incompressible air, whose parameters are also documented in Table 1.

2.3. Numerical method

2.3.1. Governing equations

In this paper, a coupled heat transfer problem between the building solid walls and the interior air is studied via a conjugate heat transfer (CHT) technique. In a CHT formulation, the governing equations for the air flow and the temperature are coupled with the heat conduction equation inside the solid. For both the fluid and the solid components, an open-source Computational Fluid Dynamics solver Nek5000 [54] is used in this study, which is based on a spectral element formulation of the governing equations [57,58]. For a conjugate heat transfer problem, the simulation domain consists of the non-overlapping fluid and solid domains with its own material properties. In this study, the solid domain corresponds to the inner and outer parts of the building envelope as described in Section 2.1, and the fluid domain corresponds to the house interior filled with air as the working fluid. A monolithic coupling approach is used, where the governing equations are solved within the fluid and solid domains simultaneously, without a need for either the sub-domain iterations, or the boundary conditions between the solid and fluid.

The governing equations for the fluid are the incompressible Navier-Stokes equations described as

$$\nabla \cdot \mathbf{u} = 0, \quad (1)$$

$$\rho \left(\frac{\partial \mathbf{u}}{\partial t} + \mathbf{u} \cdot \nabla \mathbf{u} \right) + \nabla p = \mu \Delta \mathbf{u} + \rho \mathbf{f}, \quad (2)$$

$$\rho C_p \left(\frac{\partial T}{\partial t} + \mathbf{u} \cdot \nabla T \right) = k \Delta T, \quad (3)$$

where $\rho, \mathbf{u} = \{u_x, u_y, u_z\}, \mathbf{f} = \{f_x, f_y, f_z\}, p, T, \mu, C_p$ and k are the fluid density, velocity, external force, pressure, temperature, dynamic viscosity, specific heat capacity, and thermal conductivity, respectively. A Boussinesq approximation is applied to the formulation (1)–(3), whereby the forcing term in Eq. (2) is set as $\mathbf{f} = \{0, 0, f_z\}, f_z = \beta g(T - T_0)$, where T_0 is the reference temperature taken as the initial uniform temperature of the interior air, T is the local temperature, $g = 9.8 \text{ m/s}^2$ is the gravity constant, and β is the coefficient of the thermal expansion [59].

In the solid domain, a heat conduction equation is solved as

$$\rho C_p \frac{\partial T}{\partial t} = k \Delta T, \quad (4)$$



Fig. 2. Cross sectional view of the house model taken through the center of Room 1.

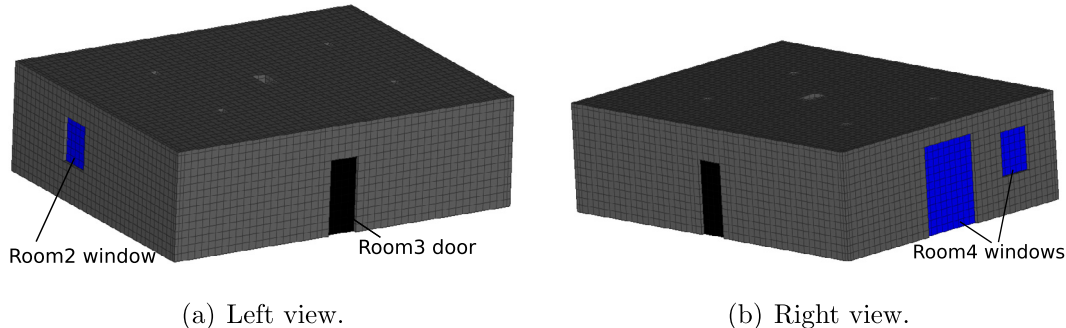


Fig. 3. Exterior view of the building envelope.

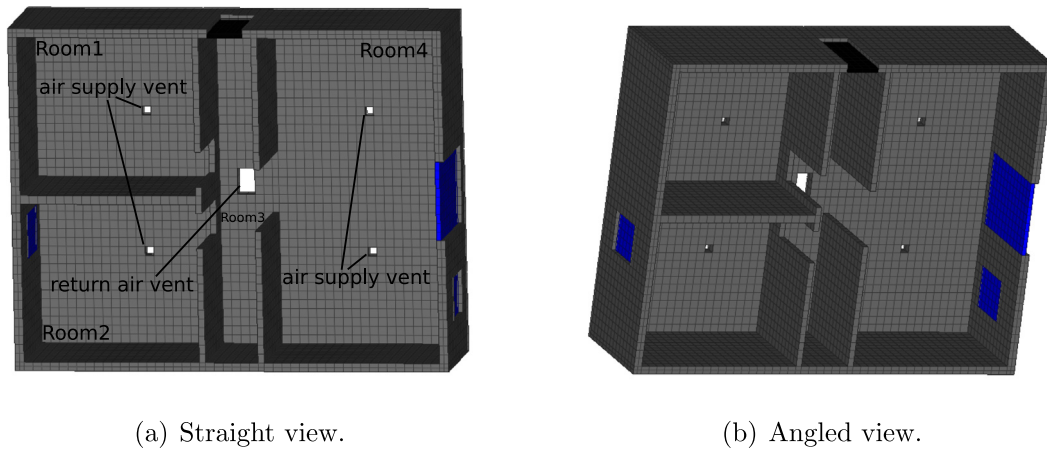


Fig. 4. Interior view of the building envelope.

Table 1
Material parameters for the solid and the fluid.

| Material | Density (ρ_s) | Specific heat capacity (C_p) | Thermal conductivity (k) | Dynamic viscosity (μ) |
|--------------------|------------------------|----------------------------------|------------------------------|---|
| Douglas Fir wood | 1200 kg/m ³ | 550 J/(kg · K) | 0.12 W/(m · K) | N/A |
| LD-C-50 spray foam | 8 kg/m ³ | 2000 J/(kg · K) | 0.038 W/(m · K) | N/A |
| Glass | 2500 kg/m ³ | 840 J/(kg · K) | 0.96 W/(m · K) | N/A |
| Air | 1 kg/m ³ | 1000 J/(kg · K) | 0.02719 W/(m · K) | 1.9×10^{-5} N · s/m ² |

where ρ is the density, C_p is the specific heat capacity, and k is the thermal conductivity of the solid. Since there are three different solid material zones in the current housing model, see Table 1, Eq. (4) is applied to each zone with its separate material parameters.

2.3.2. Numerical discretization

Eqs. (1)–(4) are spatially discretized with the spectral element method, where Lagrange–Legendre interpolating polynomials of

degree N are employed within each element as the basis functions for velocity and temperature, and the equivalent polynomials of degree $N - 2$ are used to discretize the pressure [58]. For the time advancement, an implicit second-order backward difference scheme is used for the diffusive terms, and an explicit second-order extrapolation scheme is used for the non-linear and the forcing terms. For pressure and velocity decoupling in the Navier–Stokes equations, an operator splitting approach is used [58,60],

upon which the corresponding Helmholtz and Poisson solvers are solved via a preconditioned conjugate gradient, and a generalized minimal residual method, respectively. The coupling between the fluid and the solid domains is done monolithically [55,61], where a single temperature field is composed for both the fluid and the solid domains, and the Eqs. (3) and (4) are solved simultaneously, via a preconditioned conjugate gradient method, after solving for the fluid and the pressure fields in (1), (2). The presented conjugate heat transfer model and its numerical implementation is validated in 3.1 on a laminar, two-dimensional, natural convection problem in a square enclosure compared with the simulations of [42].

2.3.3. Large Eddy Simulation

Considering the application of the presented methodology to high-Reynolds number flows associated with heating, ventilation and air-conditioning system operation, turbulent flow motions and their effect on the heat transfer must be taken into account. In the current study, a Large Eddy Simulation (LES) approach is used, with a spectral filtering regularization technique acting as a subgrid-scale model [56,62]. With the filtering-based regularization, the governing equations of the fluid motion (1)–(3) are unchanged, while the explicit filtering of primitive variables in the modal space serves to remove the energy from the unresolved subgrid scales, thus mimicking a dissipative action of classical eddy-viscosity type subgrid models [63–65]. Regularization based LES approaches are used extensively with high-order methods [56,66–68]. Specifically, a filtering-based LES model for Nek5000 was extensively validated in the previous studies for a variety of turbulent flows [55,69–71]. It is additionally validated in 3.2 for a ventilated model room test case compared to experiments [72] and LES simulations [3].

2.3.4. Model assumptions

Since a precise state of a thermal environment in a building depends on many internal and external factors and represents a complex interaction problem between physical, behavioral and environmental processes, some assumptions inevitably have to be made [30]. The current study adopts the following assumptions:

1. Interior airflow is modeled as an incompressible Newtonian buoyancy-driven fluid governed by a Boussinesq approximation, Eqs. (1)–(3).
2. Radiative heat transfer effects are not considered.
3. Solar irradiation flux is not taken into account.

The first assumption is standard in the computational studies of indoor airflow in buildings and thermal convection [4,73–76]. The last two assumptions are typical in LES studies of the built environment [3,77–80], and are related to a difficulty of implementation of radiation models in the LES framework, including the issues of the computational efficiency [35,81], parallelization [82,83], and a lack of reliable subgrid-scale models for the radiation terms [84]. Thus, inclusion of the radiation effects in the current LES model is left for future work.

2.4. Simulation details

2.4.1. Numerical grid

The residential building model described in Section 2.1 is discretized with a spectral element mesh, where element boundaries are shown in black in Figs. 1–4. As can be seen, the elements are mostly cubical, of the size 0.2 m × 0.2 m × 0.2 m, except in a few places, where specific geometrical features prevent them from being cubical, such as, for example, in the exterior solid layer, which is 0.1 m thick, or in and around the interior partitions, which are 0.14 m thick. As an example of rectangular elements, a close-up

view of the mesh around Room 4 with an instantaneous temperature snapshot superimposed is presented in Fig. 5. Similar rectangular element features are found in the other rooms. As can be seen, the choice of rectangular elements is purely due to geometrical constraints, and it has no effect on the resolved flow structures. The maximum aspect ratio of the rectangular elements in the current mesh is two, which is considered low for a numerical method to have any adverse effects related to stretched elements [60,85]. The number of elements are 22,037 in the fluid domain, and 9,715 in the solid domain, resulting in 31,752 elements total. Functions within each element are discretized with $N = 7^{\text{th}}$ order polynomials ($N = 5^{\text{th}}$ for pressure), which results in additional 8^3 interior collocation points per element (6^3 points for pressure). This yields an effective grid resolution of approximately 0.025 m in each direction, typical of the LES resolution employed in previous studies of an airflow and thermal convection in the built environment [3,78,79]. An example of the computational grid with the interior collocation points included is shown in Fig. 6; compare with Fig. 2, where the same view of the grid is shown with only the element boundaries plotted, without interior collocation points. The employed numerical grid results in approximately 16 mln. grid points for the total LES simulation. A grid convergence study is presented in Section (3.4).

2.4.2. Inlet air vent model

For the air supply vents located in the Rooms 1, 2 and 4, we consider a standard four-way deflection square vent model schematically shown in Fig. 7. To model the air flow through the four-way deflection vent, the following velocity boundary conditions are used

$$\begin{aligned} u_z &= -v, \\ u_x &= vs, u_y = 0, \text{ if } x > x_c, y > y_c, \\ u_x &= 0, u_y = -vs, \text{ if } x > x_c, y < y_c, \\ u_x &= 0, u_y = vs, \text{ if } x < x_c, y > y_c, \\ u_x &= -vs, u_y = 0, \text{ if } x < x_c, y < y_c, \end{aligned} \quad (5)$$

with the scaling factor $s \geq 0$ being equal to

$$s = \left(1 - (2l_x - 1)^2\right) \left(1 - (2l_y - 1)^2\right), \quad (6)$$

where $v = 1 \text{ m/s}$, (x_c, y_c) is the center of each air supply vent, $l_x = |x - x_c|/h$, $l_y = |y - y_c|/h$, $l_x, l_y \in [0, 1]$ correspond to the non-dimensional distances from the vent center normalized by the vent half-width, and $h = 0.1 \text{ m}$ is the half-width of each square side of the vent. The scaling factor s is used to ensure the continuity of the tangential velocity component at the junctions between the quarter partitions, where it is set to zero, as well as at the outer edges of the partitions. The positive direction of z axis is pointing upwards (from the ground to the ceiling), the positive direction of x axis is pointing from Room 1 to Room 4, and the positive direction of y axis is pointing from Room 1 to Room 2 as can be seen in the floor plan shown in Figs. 1 and 2. The model (5) thus provides the flow that spreads outward in every direction, in agreement with the operation of the actual vent. The specified inlet velocity yields 95.56 CFM airflow per air supply vent, and 382.24 CFM airflow in total for the four vents considered in the current building model.

2.4.3. Simulation setup

The current simulations model an on/off operation of the residential HVAC system, wherein each AC cycle consists of two stages: cooling stage characterized by a forced convection when AC is running, and heating stage characterized by a natural convection when AC is turned off. A variable time stepping strategy is adopted to increase the efficiency of the simulations, where the

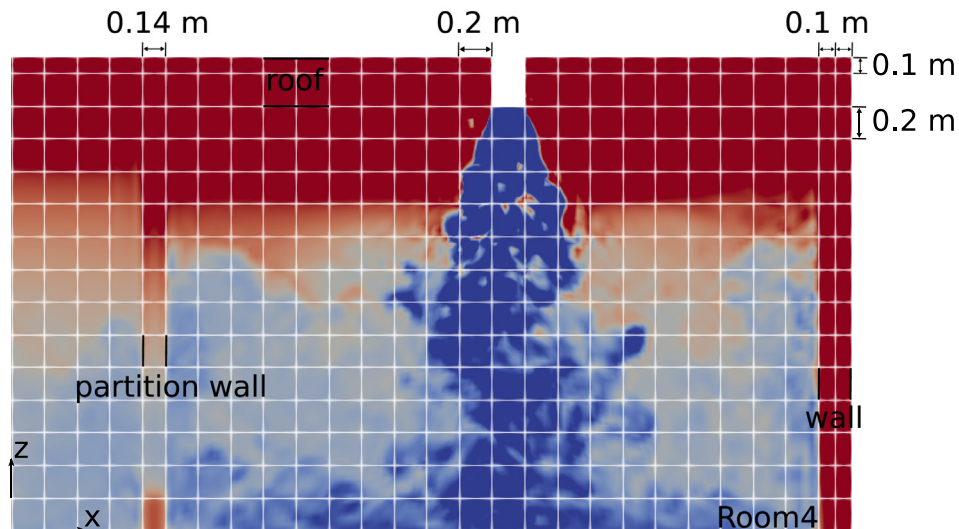


Fig. 5. Close-up view of the mesh in $x - z$ cross-sectional plane taken through the center of the air supply vent in Room 4 showing rectangular elements within the roof, exterior wall, and the inner partition. Instantaneous temperature snapshot is superimposed on the mesh. Only element boundaries are shown (no interior collocation points).

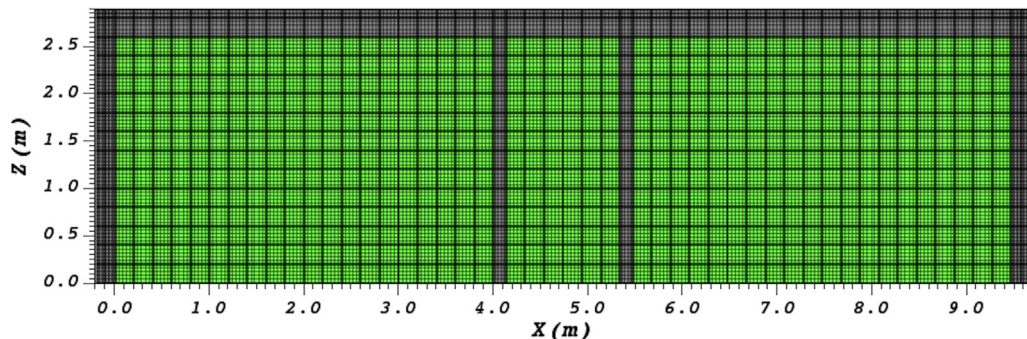


Fig. 6. A slice of the computational grid with interior collocation points included corresponding to a cross sectional view of the house model in Fig. 2.

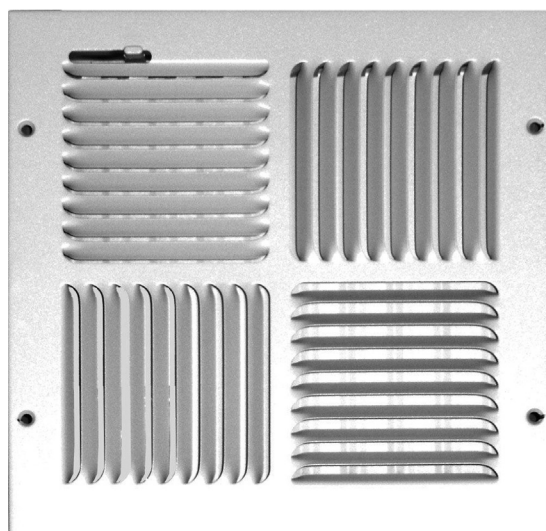


Fig. 7. A schematic of a four-way deflection square vent; modeled after Speedi Grille – 1010 CW4 ceiling vent.

time step of $\Delta t = 5 \times 10^{-4}$ s is used for a cooling stage, and $\Delta t = 2.5 \times 10^{-3}$ s is used for a heating stage. The smaller time step is required for the cooling stage in order to resolve the motions of

the small-scale turbulent eddies generated by the cooling jet associated with the short time scales. Additionally, time step needed for stability is inversely proportional to the flow velocity scale, according to the Courant-Friedrichs-Lowy condition [86], which leads to smaller time steps for the cooling stage due to a higher jet velocity. The time step can be relaxed for the heating stage, associated with the air motion by natural convection, which is slower than the forced jet flow.

Boundary Conditions. For the cooling stage, the inlet velocity given by Eq. (5) is specified at each air supply vent, with the air inlet temperature set to 60 °F (288.706 K). The air return vent in Room 3 is modeled as an outflow boundary condition during the cooling stage.

For the heating stage, the air inlet velocity at all the supply vents, and at the return vent is set to zero, with insulated boundary conditions for the temperature, modeling a shut-down of the flow through the ventilation duct. The flow during the heating stage is driven only by buoyancy force, corresponding to a situation of a natural convection.

For both stages, velocity boundary conditions at all the walls, partitions, windows and the door, are set as the no-slip. For the fluid domain, insulated temperature boundary condition is applied on the bottom floor interfacing the ground, and on the lateral walls of the air vents, while all the temperature interfaces with the building walls are handled through the conjugate heat transfer approach. For the solid domain, the temperature at the building exterior boundary Γ_{ES} , including the vertical solid walls, windows,

door and the roof, is set to $T_{ES} = T|_{\Gamma_{ES}} = 100^{\circ}\text{F}$ (310.928 K). This setup aims to model operational conditions for a residential household during an Arizona central valley summer day, where the outside temperature holds nearly constant for several hours [87,88]. A comparison of the employed isothermal boundary conditions for the building exterior surface with the convection boundary conditions (boundary conditions of the third kind) is included in Section (3.5).

Initial Conditions. Prior to a start of a regular on/off cycling of the air-conditioning equipment, the simulations undergo an initial development period. We wish to set up initial conditions, which correspond to an interior air temperature of $T_0 = 81^{\circ}\text{F}$ (300.3722 K), and an outside temperature of $T_\infty = 100^{\circ}\text{F}$ (310.928 K), to model a typical indoor environment of a residential house during the mid-day in Arizona central valley summer. However, the temperature distribution within the solid walls corresponding to these two bounding temperature points, is unknown. Ideally, one would want to set up a temperature profile within the solid walls that corresponds to a steady-state solution of the coupled heat transfer problem. But the only steady-state solution to this problem, without AC running, would correspond to an eventual heating of the interior air to 100°F , while with AC running, we can not have a steady state due to cycling. To circumvent this problem, we start with the initial conditions of the fluid at rest, interior and exterior air temperatures as specified above (81°F for interior and 100°F for exterior), and the solid wall temperature at 81°F , and we let the simulations run, with the AC turned off, until the temperature at the interface between the inner wall and the room air at a particular probe location in the center of Room 1 at a height of 1.6 m (shown in black in Fig. 1) reaches 81.5°F (300.65 K), which means that the outdoor heat started penetrating inside the building walls. To speed up the initial heating process, we also turn off a natural convection within the house, i.e. we do not consider an effect of buoyancy force during this initial stage of the simulations, whose purpose is solely to provide reasonable wall temperature profile for the initiation of the on/off cycling. This initial heating stage can be viewed as a natural heating process corresponding to a mid-morning time, when the house is still sufficiently cooled from the night, but the building envelope gradually starts heating up from the warming weather outside.

2.4.4. AC cycling control model

After this initial development stage, we start the AC cycling, originating with the cooling stage. To control the AC cycling, we consider a central air model, with a single thermostat probe located next to the center-left interior partition within the Room 3, as shown by a blue dot in Fig. 1. The thermostat probe is located 0.015 m away from the wall at a height of 1.6 m, and has a coordinate description as (4.155, 3.7, 1.6) in meters. We allow for a small offset between the thermostat probe and the wall, so it would detect the air temperature, and not the wall temperature, for more reliable readings. The deadband is set between 79°F and 81°F , i.e. AC turns off when the temperature at the probe reaches 79°F , and turns on again, when it reaches 81°F .

3. Validation

Before documenting the main results of the current study, we present a detailed validation of the computational method. First, we validate the conjugate heat transfer model versus previously published results [42]. Second, we validate the LES model on the case of a ventilated room model against experimental data [72], and the results of the LES simulations of [3]. Third, we apply the developed full house model with an on/off HVAC control to the case study presented in [10], and compare Nek5000 results with

both the field data, and the EnergyPlus simulations documented in [10]. We also perform a grid convergence study, and an analysis of the sensitivity of the simulations to the exterior building wall boundary condition. Validation of the constituent physical modules of the solver on the test problems, combined with grid refinement studies, is a reliable practice for validation of CFD models in the analysis of flow and heat transfer in and around buildings [89–91].

3.1. Validation of conjugate heat transfer model

To validate the conjugate heat transfer model in Nek5000, a two-dimensional, laminar, natural convection flow in a square enclosure is simulated and compared with the previous numerical results of [42].

Fluid domain is a square with coordinates $[0, 1] \times [0, 1]$ that defines a characteristic length $L = 1$, and solid domain is an adjacent rectangle with the thickness of 0.2 attached to the right boundary of the fluid domain at $[1, 1.2] \times [0, 1]$, as can be seen in Fig. 8(a). The fluid-solid interface is a vertical line from (1, 0) to (1, 1) shown in black in Fig. 8(a). In the simulation, following [42], all the parameters are set to be non-dimensional with $\rho = 1$, $\mu = 1$, $C_p = 1$, and $k = 1/0.7$ for the fluid and the solid.

The initial condition is at rest with $T_0 = 0$. The lower horizontal wall from (0, 0) to (1.2, 0), and the upper horizontal wall from (0, 1) to (1.2, 1) are insulated. Isothermal temperature boundary conditions are defined on the left vertical wall from (0, 0) to (0, 1) with $T_C = 0$, and on the right vertical wall from (1.2, 0) to (1.2, 1) with $T_H = 1$. Grashof number $Gr = g\beta(T_H - T_C)L^3\rho^2/\mu^2$, is set to be 10^3 , 10^4 , 10^5 , 10^6 and 10^7 , as in [42]. The numerical mesh, which is shown in Fig. 8(a), is uniform and consists of square elements of the size 0.2×0.2 employing 5th-order polynomial basis functions for velocity and temperature within each element.

The time step size in Nek5000 simulations is set to 10^{-3} , 10^{-4} , 10^{-4} , 10^{-5} , for the four values of the Gr number, respectively. Since the results in Ref. [42] are from a steady state model, and our simulations are transient, the results from Nek5000 are presented at the time $t = 2$, when the flow has reached a steady state. The comparison of the normalized temperature at the fluid-solid interface between the current simulations and Ref. [42] is shown in Fig. 8(b) and in Table 2, and an excellent agreement is observed. In Table 2, we present the mean error $\bar{\epsilon}$, the root-mean square standard deviation σ , and the percent relative error, $\bar{\epsilon}_{rel}$, defined as

$$\bar{\epsilon} = \frac{\sum_{i=1}^N |D_i^{current} - D_i^{ref}|}{N}, \quad (7)$$

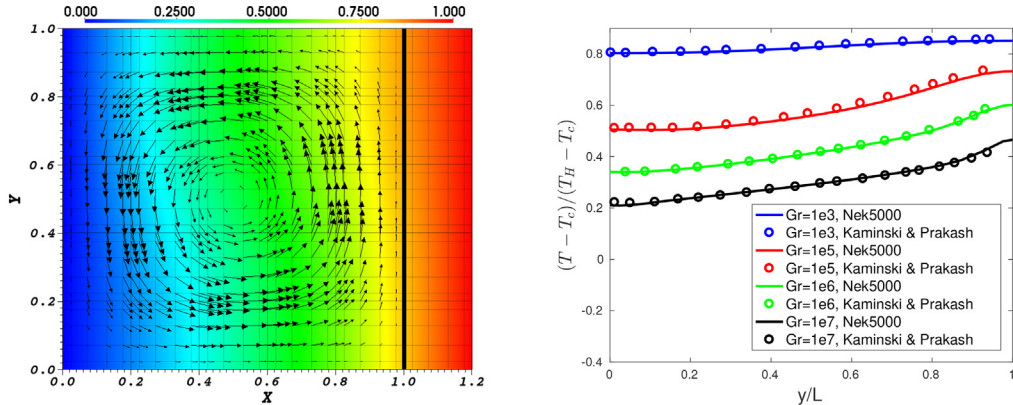
$$\sigma = \sqrt{\frac{\sum_{i=1}^N (|D_i^{current} - D_i^{ref}| - \bar{\epsilon})^2}{N}}, \quad (8)$$

$$\bar{\epsilon}_{rel} = \frac{\bar{\epsilon}}{|\bar{D}_{ref}|}, \quad (9)$$

where D stands for the data to be compared (normalized temperature from Fig. 8(b) in this case), superscript “*current*” refers to the current data, superscript “*ref*” refers to the reference data, N is the number of samples available for comparison, and \bar{D}_{ref} in Eq. (9) stands for an average value of the reference data.

3.2. Validation of Large Eddy Simulation model

The validation of the presented Large Eddy Simulation model is performed using a test case of a ventilated model room against



(a) Temperature distribution and velocity vectors at $Gr = 1000$ at time $t = 2$ from Nek5000. Numerical mesh showing the elements and the collocation points is also plotted.

Fig. 8. Visualization and comparison of data for conjugate heat transfer validation test case with the data from Ref. [42].

Table 2

Quantitative comparison of temperature data for the conjugate heat transfer validation test case with the data from Ref. [42].

| Data | Mean square error, $\bar{\epsilon}$ | STD, σ | Relative error, $\bar{\epsilon}_{rel}$ % |
|------------|-------------------------------------|---------------|--|
| $Gr = 1e3$ | 0.0041 | 0.0012 | 0.4953 % |
| $Gr = 1e5$ | 0.0099 | 0.0027 | 1.6883 % |
| $Gr = 1e6$ | 0.0015 | 0.0016 | 0.3447 % |
| $Gr = 1e7$ | 0.0039 | 0.0039 | 1.2942 % |

experimental data [72] and the LES simulations in [3]. The model room corresponds to a rectangular box with the floor area of $0.914 \text{ m} \times 0.457 \text{ m}$ and the height of 0.305 m , with a 0.03 m thick wall partition of a height 0.15 m located in the middle of the room. The ceiling of the room features one air inlet and one air outlet, both of the size $0.1 \text{ m} \times 0.1 \text{ m}$. A steady plug flow with the velocity of 0.235 m/s is specified at the inlet. Based on the inlet velocity and the inlet width, the Reynolds number of the inlet airflow is 1500. All geometrical and physical parameters of the study are taken exactly as in the references [72,3]. The numerical mesh consists of cuboid elements of the average size $0.13 \text{ m} \times 0.15 \text{ m} \times 0.15 \text{ m}$, which are correspondingly refined near the location of the air vents to conform to the geometry. Following [3], we run the simulations with the time step of $\Delta t = 0.05 \text{ s}$, for 2000 time steps, upon which a statistical information is collected for 10,000 time steps, corresponding to 500 s in physical time. Fig. 9 illustrates a mean airflow pattern in the room by plotting time-averaged velocity magnitude with the superimposed in-plane velocity vectors, where the Nek5000 computational grid including the elements and the collocation points is also shown.

Fig. 10(a) compares time-averaged profile of vertical velocity along the center of the vertical inlet jet with the experiments [72] and the simulations [3], while Fig. 10(b) compares time-averaged vertical velocity profile along the horizontal line at the mid-partitioned height and the mid-plane. Quantitative comparison of data is presented in Table 3, where the definition of errors is the same as in Eqs. (7)–(9), and the data D stands for the vertical velocity at the respective locations. In both cases, an excellent agreement is obtained. Note that a high value of percent relative

(b) Temperature comparison at the fluid-solid interface between the current simulations at $t = 2$ and Ref. [42].

error in Fig. 10(b) is due to a division by an average value in Eq. (9), which in this case is close to zero, precisely, 0.0402.

3.3. Validation of house HVAC control model

In this section, we present a validation of our residential house model with the on/off HVAC temperature control implemented according to the strategy described in Section 2.4.4. We compare our simulations with both the field data and the EnergyPlus simulations documented in Ref. [10]. The data in Ref. [10] is for a single story medium-size residential house located in Sacramento, CA [92]. Sacramento, CA, the same as Phoenix, AZ, are both located in the Building America “hot-dry” climate zone [93]. The data for the field study was collected in the month of August, when the largest cooling loads occur [10]. For the validation of our AC cycling model, we chose to compare with the day-time temperature data of Ref. [10] corresponding to the time period between 10 am and 3 pm, when AC was running using an on/off temperature control, with a constant thermostat setpoint set to 70.52°F (corresponding to an upper bound of a deadband) and a deadband interval of 1.8°F . Since every building has different thermal mass characteristics, following [10], we adjust the thermal mass to match the observed fluctuation of interior temperatures when the HVAC system is both on and off.

A comparison of the indoor temperature in our simulations with the field data and EnergyPlus simulations of Ref. [10] is shown in Fig. 11. Fig. 11 shows a good agreement of Nek5000 data with both the field data and EnergyPlus simulations with on/off model. It can also be observed that the omission of on/off model in EnergyPlus simulations completely misses the cyclic temperature behavior as described in Ref. [10], showing the importance of inclusion of the dynamic HVAC control models into the building simulation software. Note that since the geometry and the setup of the model house are not the same in the current work and in Ref. [10], we do not expect a one-to-one correspondence between the data, but rather an agreement in the overall trends with respect to a temperature variation during the cooling and heating cycles, as well as the average cycle dynamics. It is interesting to note that the

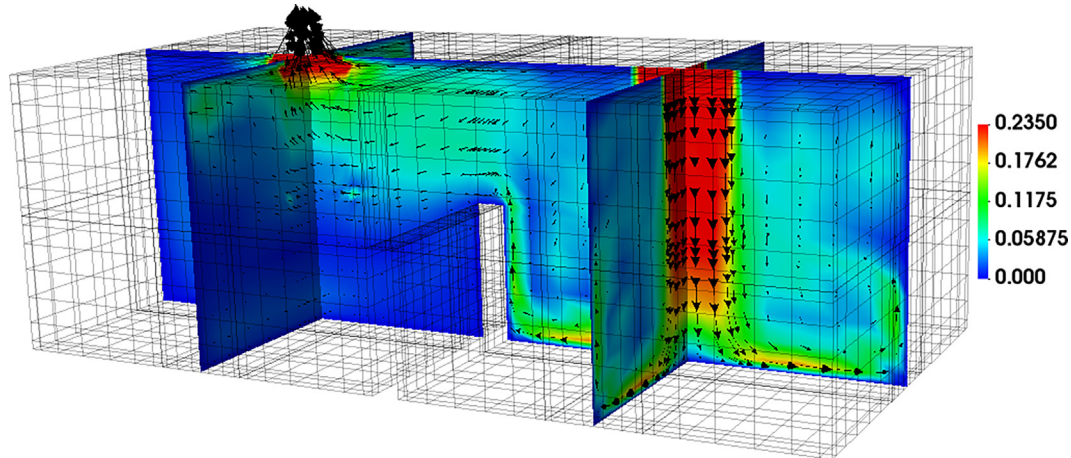
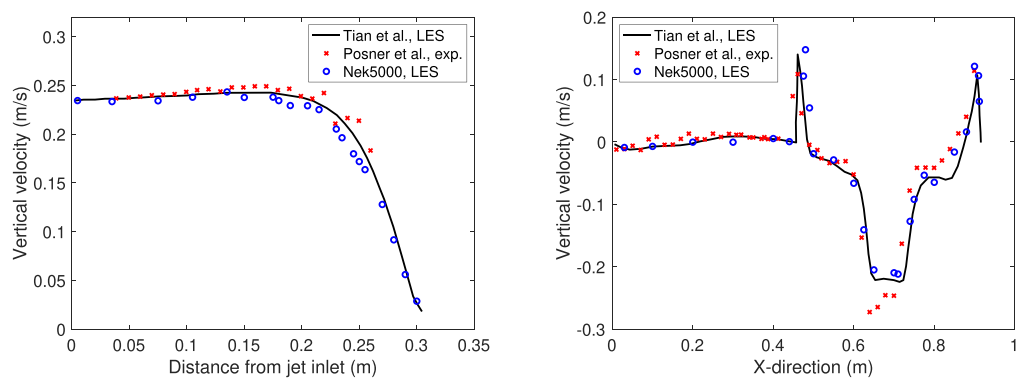


Fig. 9. Time-averaged velocity magnitude with the superimposed in-plane velocity vectors for the ventilated room validation test case with Nek5000. Velocity is in m/s. Computational grid including elements and collocation points is also shown.



(a) Vertical velocity along the center of the vertical inlet jet.
(b) Vertical velocity along the horizontal line at the mid-partitioned height and the mid-plane.

Fig. 10. Comparison of time-averaged velocity profiles for the ventilated room validation test case with the data from Refs. [72,3].

Table 3

Quantitative comparison of vertical velocity data for the ventilated room validation test case with the data from Ref. [3].

| Data | Mean error, $\bar{\epsilon}$ | STD, σ | Relative error, $\bar{\epsilon}_{rel}$ % |
|------------|------------------------------|---------------|--|
| Fig. 10(a) | 0.0083 | 0.0060 | 4.1978 % |
| Fig. 10(b) | 0.0204 | 0.0257 | 50.7472 % |

temperature reaches the values higher than the deadband for the field data, while it is controlled more precisely in both Nek5000 and EnergyPlus simulations. This might be due to the fact that the original field study did not install a sensor next to the thermostat to confirm setpoint values as thermostat can have an uncertainty of 1–2 °F [10]. Another possible reason is that the averaged room temperature between the living room, master bedroom and the den is plotted for the field data in Ref. [10], with the den, located quite far from a thermostat and not having its own cooling vent, potentially contributing to higher measured temperatures. In EnergyPlus, the on/off AC switch is controlled directly by the mean zone temperature and not by a temperature from a pointwise sensor location, while in Nek5000, Room 3 (whose temperature is plotted) and the thermostat are located close to each other, and

there is no physical thermostat uncertainty in the simulations, explaining a better agreement in temperature values between the two numerical models, rather than between the field data and the two models. A quantitative comparison between the Nek5000 results and the data from Ref. [10] is presented in Table 4. It is seen that the mean value for the duration of both cooling and heating cycles agrees well between Nek5000, EnergyPlus and the field data. A good agreement in variability is also noted, apart from a high value of cooling variability in the field data, which can be associated with the uncertainty in a thermostat setpoint temperature, as mentioned above.

3.4. Grid convergence study

This section demonstrates the grid convergence study for the full house computational model described in Section 2.4.1. Specifically, we compare an employed mesh using 16 mln. grid points, corresponding to $N = 7^{th}$ polynomial order, to a coarser mesh of 10.7 mln. grid points, corresponding to $N = 6^{th}$ polynomial order. A comparison is performed for a cooling stage of the cycles 14 and 15 and is presented in Fig. 12. As can be seen from the figure,

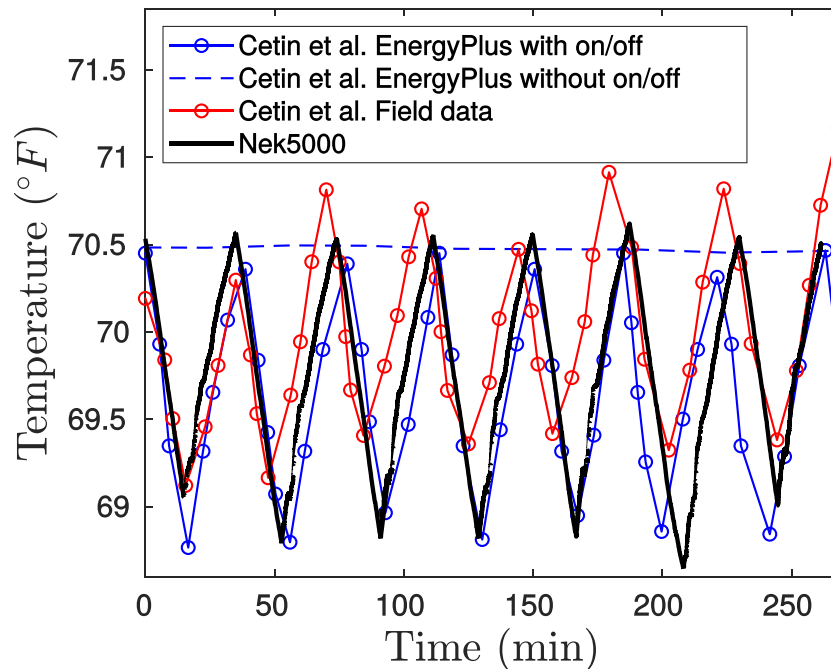


Fig. 11. Comparison of the interior temperature fluctuations with the on/off AC control between the current simulations and the field data of Cetin et al. [10] and the EnergyPlus simulations with and without on/off AC control [10]. Horizontally-averaged temperature in Room 3 at the thermostat level is plotted for Nek5000; data for the field measurements and EnergyPlus are as described in [10].

Table 4

Quantitative comparison of data for the cooling and heating cycles duration and variability between the current house HVAC simulations, the field data of Cetin et al. [10], and the EnergyPlus simulations of Cetin et al. [10].

| Data | Cooling Average (min) | Cooling STD, % | Heating Average (min) | Heating STD, % |
|-------------------------------------|-----------------------|----------------|-----------------------|----------------|
| Cetin et al. EnergyPlus with on/off | 16.6968 | 10.49% | 20.8929 | 6.8% |
| Cetin et al. Field data | 16.7857 | 22.02% | 21.5179 | 7.09% |
| Nek5000 | 17.0944 | 11.01% | 20.2584 | 7.36% |

the results are very close, with the maximum deviation of less than 2%, which confirms that the original grid is sufficiently refined.

3.5. Sensitivity to external wall temperature boundary conditions

As mentioned in Section 2.4.3, the current computational model uses isothermal boundary conditions for the exterior surface of the building walls. In this section, we compare the isothermal boundary conditions with the convection boundary conditions, also known as the boundary conditions of the third kind, frequently used in the simulations of the building environment [30,34]. We would, however, like to note that in the aforementioned references, the convection boundary conditions were used on the exterior building walls, which were modeled as zero-thickness virtual dividers between the interior and the exterior air, i.e., without a conjugate heat transfer modeling. Nonetheless, a comparison between the two types of boundary conditions as applied to the exterior surface of a finite-thickness building wall in the current CHT approach is presented below.

Convection boundary conditions are described by the following equation

$$-k\nabla T \cdot \hat{n} = h_c(T - T_\infty), \text{ on } \Gamma_{es}, \quad (10)$$

where T is the unknown temperature on the external solid boundary Γ_{es} , \hat{n} is the outward unit surface normal, k is thermal conductivity of the solid, T_∞ is the ambient temperature outside the building, and h_c is the convective heat transfer coefficient governing

the heat flux between the building surface and the ambient surroundings. Consistent with the isothermal formulation, we set the external temperature $T_\infty = 50^\circ\text{F}$ (310.928 K). Convective heat transfer coefficient is defined to be $h_c = 50 \text{ W}/(\text{m}^2\text{K})$, which is typical for a forced convection in air [94,95], and the coefficient of thermal conductivity k for each material is as specified in Table 1.

Comparison is presented in Fig. 13 for both the cooling and the heating stages for cycles 14 and 15. It can be seen that the differences introduced by the changes in boundary conditions are insignificant. The temperature profiles obtained with the two boundary conditions are essentially identical for the entire duration of the heating cycle, and for most of the cooling cycle. A slight deviation in the end of the cooling cycle is most likely related to a chaotic turbulent state associated with the late stages of mixing between the cooling jet and the warm interior air. Thus, this difference is more likely associated with a different realization of a turbulent state, rather than being solely attributed to the effect of boundary conditions. We thus conclude that isothermal boundary conditions for the exterior wall surface temperature represent an adequate approximation in the current study.

4. Results

Having validated our conjugate heat transfer LES-HVAC simulation model using benchmark problems, field data, and a grid independence test, we now apply the methodology to simulate a case study of a residential house model in Phoenix, AZ, presented in Section 2.1. As opposed to field measurements, which are hard to

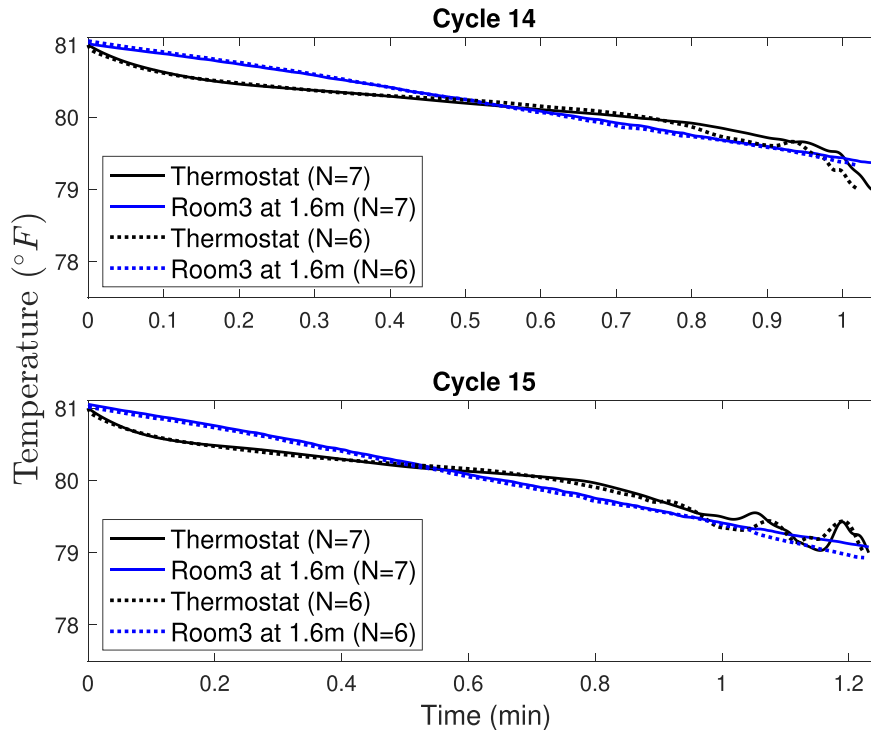
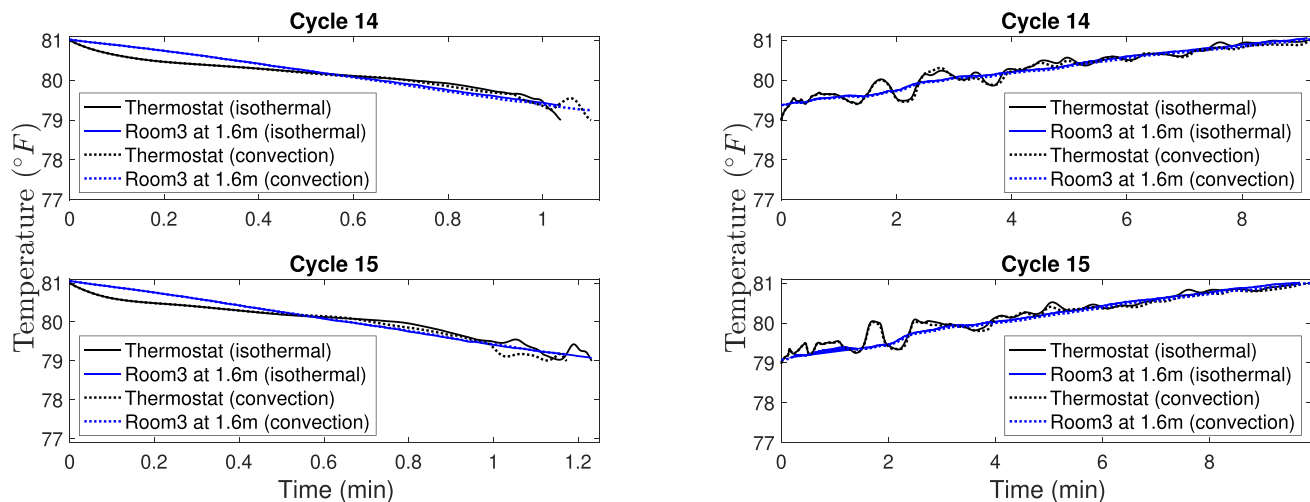


Fig. 12. Results of the grid convergence study. Thermostat readings (black) and horizontally-averaged temperature in Room 3 at the thermostat level (blue) with $N = 7^{\text{th}}$ order polynomials (original mesh, 16 mln. grid points) and $N = 6^{\text{th}}$ order polynomials (coarser mesh, 10.7 mln. grid points) for a cooling stage of cycles 14 and 15.



(a) Cooling stage for cycles 14 and 15.

(b) Heating stage for cycles 14 and 15.

Fig. 13. Comparison of horizontally-averaged temperature in Room 3 at the thermostat level (blue lines), and the thermostat readings (black lines), for the isothermal (solid lines) and convection (dashed lines) boundary conditions on the external solid wall surfaces. (For interpretation of the references to color in this figure legend, the reader is referred to the web version of this article.)

obtain in more than a few selected sensor locations, and to Energy-Plus simulations which only output the mean zone temperature, the advantages of our CFD approach is that the entire transient temperature field inside the house is available and can be easily probed.

4.1. Cooling and heating cycles

The total time of the simulations consists of an initial heating stage, followed by 30 cooling and heating cycles, which corre-

sponds to the total of 467.37 min of physical time, or approximately 7.8 h. The breakdown of the total simulation time into the heating and cooling stages, as well as the initial stage, is presented in Table 5. It can be seen that the initial heating stage, which heats the inner wall by only 0.5 °F, takes 108.5 min, or 1.8 h, which testifies of rather long time scales associated with the solid heat transfer process due to relatively high thermal mass (ρC_p) of the exterior wood wall. One can notice from Table 5 that the cooling stage occupies only 7.8% of the total elapsed time, signifying an extreme importance of incorporating AC idling and nat-

Table 5

Simulation time and percent breakdown between different stages.

| Stage | Initial heating | Total cycle cooling | Total cycle heating | Total |
|------------------|-----------------|---------------------|---------------------|--------|
| Time, min. | 108.5 | 36.69 | 322.18 | 467.37 |
| Percent of total | 23.2% | 7.8% | 69% | 100% |

ural heating effects into the HVAC operation and building energy models, since no energy is consumed when AC is turned off, which corresponds to 90% time in the combined cycle.

Table 6 gives a detailed breakdown of the cooling and heating time spent in each AC cycle for the 30 cycles simulated. For a convenience of analysis, we break the cycles into the three groups of 10 cycles each. It can be seen that the heating time is significantly reduced between Group 1 (1–10 cycles) and Group 2 (11–20 cycles), while it is further reduced for Group 3 (21–30 cycles), but only slightly. Cooling time is slightly reduced between Group 1 and Group 2, while it is essentially unchanged for Group 3. To better illustrate these effects, **Fig. 14** presents the bar plots for the calculated cooling and heating time periods. It can be clearly seen that the first 10 cycles correspond to the most significant reduction in the average cycle time both for cooling and for heating cycles, although the effect is more significant for heating than for cooling. This reduction in the average duration of the cooling and heating cycles, although similar in its perceived outcome, is caused by different phenomena. For the cooling, it corresponds to a better cooling efficiency once the cooling air gets better mixed with the warm room air. The reduction in the heating cycles is, however, due to a gradual heating of the building envelope by the outside air, which acts to increase the inner wall temperature and, thus, leads to a higher heat transfer rate through the building walls. These two different reasons can also explain why the cooling cycles stabilize after the first 10 cycles, while the heating cycles keep decreasing in time. The cooling cycles stabilize once the air is mixed to a sufficient degree, which yields a flow pattern that no longer significantly changes between cooling cycles. However, the heating cycles keep decreasing in time, because the building wall continues to heat, although the rate of this heating diminishes once the temperature gradient inside the solid wall starts approaching a constant value.

We can also notice a significant variability in the cooling and heating times, which is further illustrated in **Table 7**, which lists the average value, the standard deviation, and the standard deviation as the percent of the average value, calculated separately for each Groups 1 to 3. It can be seen that the variability is especially pronounced during the first 10 cycles, reaching as much as 20.7% for cooling and 26% for heating. However, Groups 2 and 3, while keeping relatively unchanged mean values, demonstrate 7–13% variability, which is significant, especially in a consideration of electric grid stability and demand response. In comparison with the field and EnergyPlus data of Cetin et al. [10] in **Table 4**, the variability levels in Groups 2 and 3 agree very well with these data.

Additionally, cooling variability is typically higher than the heating variability, the trend that can also be observed in the field data, due to the reasons explained below in Section 4.2. Variability of cycles in Group 1, which is in the early stages of the simulations, is related to a rapid drop in the mean heating cycle times as the house gets heated from the walls, which explains both the high values of variability in Group 1, and the fact that the heating variability is higher than the cooling variability in this group. To further understand the nature of this variability, **Table 8** documents the percent deviation for each cooling and heating cycle from their corresponding in-group mean value. Surprisingly, it can be seen that, the positive and negative fluctuations from the mean in both cooling and heating cycles typically, but not always, correlate with each other, i.e., if we had a significantly shorter cooling cycle, it is very likely that the following heating cycle will be shorter as well. To test this hypothesis, we compute the percent deviation for the duration of each cycle from the previous cycle in **Table 9**, defined as $\Delta t_c = (t_c^{\text{current}} - t_c^{\text{previous}})/t_c^{\text{previous}} \times 100\%$ for cooling, and $\Delta t_h = (t_h^{\text{current}} - t_h^{\text{previous}})/t_h^{\text{previous}} \times 100\%$ for heating. **Fig. 15** documents the quadrant plot of the cooling and heating time deviations $\Delta t_c, \Delta t_h$. It can be seen from the figure that almost all the data falls into the Quadrants 1 or 3, meaning that we have a very good correlation between the same-sign deviations for the cooling and heating time periods from the previous cycle, and, indeed, the computed correlation coefficient is $R = 0.92$. The exception to this rule are three cycles within the first group, when the flow is still in a developmental stage, and Cycle 28, which is an outlier due to a chaotic nature of turbulence. Thus, while it might be tempting to conclude that the shorter cooling cycles are beneficial because they save energy, it must be kept in mind that the follow-up heating cycle will likely be short as well, so that the time duration until the next energy consumption period is shortened, which negates the perceived original energy benefit. It will be shown in the next section that both positive and negative time fluctuations from the mean are caused by the temperature fluctuations at the thermostat level created by the turbulent motions associated with the interaction of the cooling jet and the in-room air.

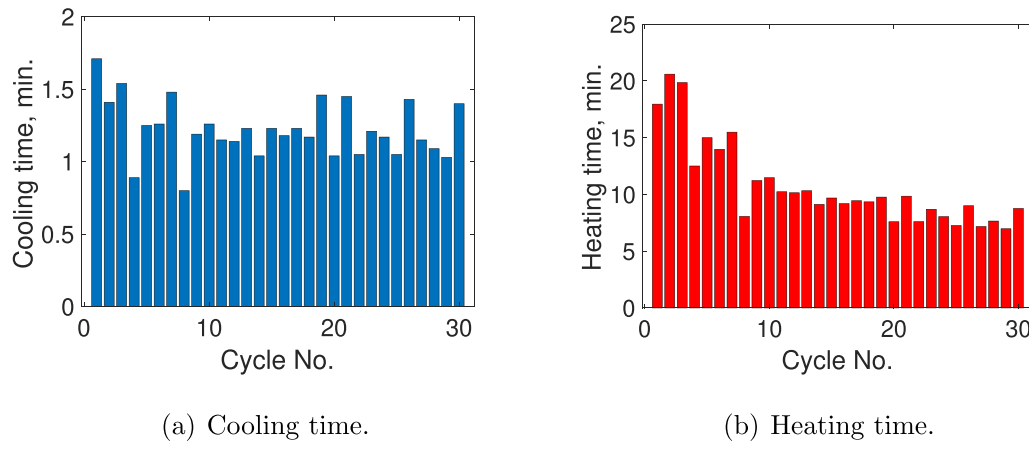
4.2. Thermostat readings

To further understand the nature of the cycle-to-cycle variability, in this section we examine the temperature signal as obtained from the thermostat probe during the cooling and heating periods for two representative cycles. We choose to compare cycles 25 and

Table 6

Cooling and heating time consumption in minutes for the 30 cycles.

| Cycle No. | 1 | 2 | 3 | 4 | 5 | 6 | 7 | 8 | 9 | 10 | Total |
|--------------|-------|-------|-------|-------|-------|-------|-------|------|-------|-------|--------|
| Cooling time | 1.71 | 1.41 | 1.54 | 0.89 | 1.25 | 1.26 | 1.48 | 0.80 | 1.19 | 1.26 | 12.79 |
| Heating time | 17.96 | 20.60 | 19.86 | 12.51 | 15.01 | 13.98 | 15.49 | 8.07 | 11.23 | 11.48 | 146.19 |
| Cycle No. | 11 | 12 | 13 | 14 | 15 | 16 | 17 | 18 | 19 | 20 | Total |
| Cooling time | 1.15 | 1.14 | 1.23 | 1.04 | 1.23 | 1.18 | 1.23 | 1.17 | 1.46 | 1.04 | 11.87 |
| Heating time | 10.24 | 10.15 | 10.33 | 9.13 | 9.69 | 9.20 | 9.45 | 9.35 | 9.77 | 7.60 | 94.91 |
| Cycle No. | 21 | 22 | 23 | 24 | 25 | 26 | 27 | 28 | 29 | 30 | Total |
| Cooling time | 1.45 | 1.05 | 1.21 | 1.17 | 1.05 | 1.43 | 1.15 | 1.09 | 1.03 | 1.40 | 12.03 |
| Heating time | 9.85 | 7.61 | 8.70 | 8.05 | 7.27 | 9.01 | 7.18 | 7.66 | 6.98 | 8.77 | 81.08 |

**Fig. 14.** Bar plot of the cooling and heating time periods within the simulated 30 cycles.**Table 7**

Average value and standard deviation for the cooling and heating time periods for the 30 cycles.

| Cycle No. | 1–10 | Average, min. | STD, min. | STD, % |
|--------------|-------|---------------|-----------|---------|
| Cooling time | | 1.28 | 0.28 | 20.71 % |
| Heating time | | 14.62 | 4.00 | 25.99 % |
| Cycle No. | 11–20 | Average, min. | STD, min. | STD, % |
| Cooling time | | 1.19 | 0.12 | 9.50% |
| Heating time | | 9.49 | 0.79 | 7.91 % |
| Cycle No. | 21–30 | Average, min. | STD, min. | STD, % |
| Cooling time | | 1.20 | 0.16 | 13.01% |
| Heating time | | 8.11 | 0.94 | 10.98 % |

Table 8

Percent deviation from the in-group mean for the cooling and heating time periods.

| Cycle No. | 1 | 2 | 3 | 4 | 5 | 6 | 7 | 8 | 9 | 10 | Mean |
|--------------|--------|---------|--------|---------|---------|--------|---------|---------|---------|---------|------------|
| Cooling time | 33.70% | 10.24% | 20.41% | -30.41% | -2.27% | -1.49% | 15.72% | -37.45% | -6.96% | -1.49% | 1.28 min. |
| Heating time | 22.85% | 40.91% | 35.85% | -14.43% | 2.67% | -4.37% | 5.96% | -44.80% | -23.18% | -21.47% | 14.62 min. |
| Cycle No. | 11 | 12 | 13 | 14 | 15 | 16 | 17 | 18 | 19 | 20 | Mean |
| Cooling time | -3.12% | -3.96% | 3.62% | -12.38% | 3.62% | -0.59% | 3.62% | -1.43% | 22.30% | -12.38% | 1.19 min. |
| Heating time | 7.90% | 6.94% | 8.84% | -3.80% | 2.10% | -3.07% | -0.43% | -1.490% | 2.94% | -19.92% | 9.49. min. |
| Cycle No. | 21 | 22 | 23 | 24 | 25 | 26 | 27 | 28 | 29 | 30 | Mean |
| Cooling time | 20.53% | -12.72% | 0.58% | -2.74% | -12.72% | 18.87% | -4.41% | -9.39% | -14.38% | 16.38% | 1.20 min. |
| Heating time | 21.48% | -6.14% | 7.30% | -0.72% | -10.34% | 11.12% | -11.42% | -5.53% | -13.91% | 8.16% | 8.11 min. |

Table 9Percent deviation for each cycle from the previous cycle for the cooling and heating time periods, Δt_c and Δt_h .

| Cycle No. | 1 | 2 | 3 | 4 | 5 | 6 | 7 | 8 | 9 | 10 |
|--------------|---------|---------|--------|---------|---------|--------|---------|---------|--------|---------|
| Cooling time | N/A | -17.54% | 9.22% | -42.21% | 40.45% | 0.8% | 17.46% | -45.95% | 48.75% | 5.88% |
| Heating time | N/A | 14.70% | -3.56% | -37.00% | 19.98% | -6.86% | 10.80% | -47.90% | 39.16% | 2.22% |
| Cycle No. | 11 | 12 | 13 | 14 | 15 | 16 | 17 | 18 | 19 | 20 |
| Cooling time | -8.73% | -0.87% | 7.89% | -15.44% | 18.27% | -4.07% | 4.24% | -4.88% | 24.79% | -28.77% |
| Heating time | -10.80% | -0.88% | 1.77% | -11.62% | 6.13% | -5.06% | 2.71% | -1.06% | 4.49% | -22.21% |
| Cycle No. | 21 | 22 | 23 | 24 | 25 | 26 | 27 | 28 | 29 | 30 |
| Cooling time | 39.42% | -27.59% | 15.24% | -3.31% | -10.26% | 36.19% | -19.58% | -5.22% | -5.50% | 35.92% |
| Heating time | 29.60% | -22.74% | 14.32% | -7.47% | -9.69% | 23.93% | -20.31% | 6.68% | -8.88% | 25.64% |

26, which exhibit a large negative, and large positive, time fluctuations, respectively. Fig. 16 shows the temperature readings at the thermostat probe as compared to the temperature in the Rooms 1–4 averaged over horizontal planes at the thermostat height of $z = 1.6$ m. For a reference, we also plot the room temperatures averaged over a height of $z = 1$ m and $z = 0.2$ m, respectively.

We see from Fig. 16(a) that at the end of the cooling cycle the thermostat probe signal exhibits a large negative fluctuation from the corresponding Room 3 averaged temperature at that height, making a temperature at the thermostat reach the lower bound of a deadband of 79 °F early, thus ending the cooling cycle early. Note that, due to an early termination of the cycle, the actual Room

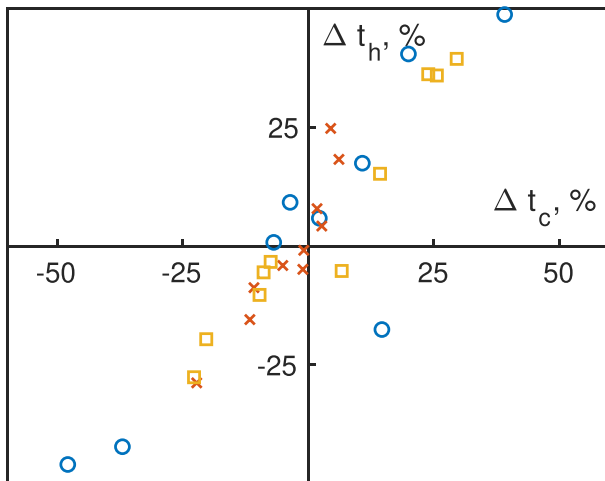


Fig. 15. Correlation between cooling and heating time deviations for each cycle from the previous cycle, Δt_c and Δt_h . Blue circles correspond to the data in Group 1, red crosses in Group 2, and yellow squares in Group 3. (For interpretation of the references to color in this figure legend, the reader is referred to the web version of this article.)

3 temperature is actually at a higher value than 79 °F at the end of the cycle 25. This also explains the shortening of the follow-up heating cycle, since Room 3 now needs to heat up by a smaller amount during the heating stage, since it starts with an elevated temperature at the beginning. For the cycle 26, where we have a positive shift in a cooling time duration, the situation is reversed – the thermostat probe encounters a large positive temperature fluctuation, which makes the AC unit keep cooling longer, with the resulting end-of-the-cycle averaged Room 3 temperature lower than the deadband value of 79 °F. As a result, the heating cycle needs to compensate for this overshoot, allowing the room to heat for a longer time.

Fig. 16 also shows that the temperature variability is the most significant at the end of the cooling cycle and the beginning of the heating cycle, when the cooling air reaches the thermostat location and results in large temperature fluctuations due to a strong turbulent mixing between the cold and warm air regions. When the AC is turned off, the effects of the turbulent mixing associated with the forced convection gradually disappear, and, once the natural convection sets up, it results in a more uniform temperature distribution across the given horizontal planes throughout the entire house, as can be seen by a very good collapse of the temperature plots across all the rooms at any given height during the later part of the heating cycle. We can thus conclude that the variability in the duration of the cooling cycles results from the turbulent nature of the cooling jet flow, while variability in the duration of the heating cycles is rather attributed to the over- or undershoots of a preceding cooling cycle, and not to the temperature fluctuations due to turbulence. This explains a relatively higher value of variability for the cooling cycles as compared to the heating cycles.

4.3. Remote room temperature probes

We now turn to examine the individual room temperatures that are established during the operation of the current HVAC system model with a central thermostat control setting. From Fig. 16 we see that the average temperature of Room 3 is typically higher during the cooling cycle than the temperature within the living room (Room 4) and the bedrooms (Rooms 1 and 2), since the thermostat is located in the hallway, which does not have its own air supply vent. This leads to the fact that Rooms 1, 2 and 4 typically experience colder temperatures at the end of the cooling cycle than that

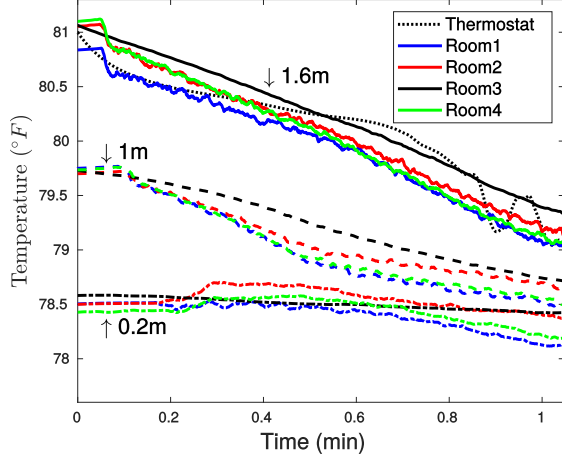
set by a thermostat setpoint, which can clearly be seen in Fig. 16 (a). From the data, we can infer that this overcooling occurs for most of the cycles, that is for all the cycles with positive, near-zero, and even some negative fluctuations in duration, as can be seen, for example, in Fig. 17, where cycles 14 and 24, both with negative fluctuations in duration, are plotted. The overcooling leads both to an excessive use of energy, when the rooms are cooled by an amount larger than needed, and to a reduced thermal comfort.

To propose a possible remedy, we investigate a potential efficiency of remote room sensors, which can be used either for a multi-zone control, or for a smart control of a central thermostat. Thus, we place remote sensor probes into the Rooms 1, 2 and 4, referred to as Probes 1, 2, 3. Probes 1, 2, 3, shown in red in Fig. 1, are located, correspondingly, at (0.4, 0.4, 1.6), (0.4, 7, 1.6), and (6.28, 6.6, 1.6), which is away from each air supply vent and not too close to the walls, for reliable temperature readings. Fig. 18 compares the readings of the remote sensor probes with the room averaged temperatures taken over the same height of 1.6 m for the cycles 25 and 26. While turbulent fluctuations, especially at the end of the cooling cycle and the beginning of the heating cycle, as observed previously, are still pronounced, it can be seen, that on average, the remote sensor probes can track the local room temperatures fairly well, thus offering a promising technology for a smart house HVAC control. While it is expected that a decentralized temperature control system can substantially enhance a thermal comfort of the building occupants and reduce the energy usage by eliminating unnecessary overcooling of the interior spaces, its effect on eradicating or reducing the AC cycle variability is unknown, and needs further investigation.

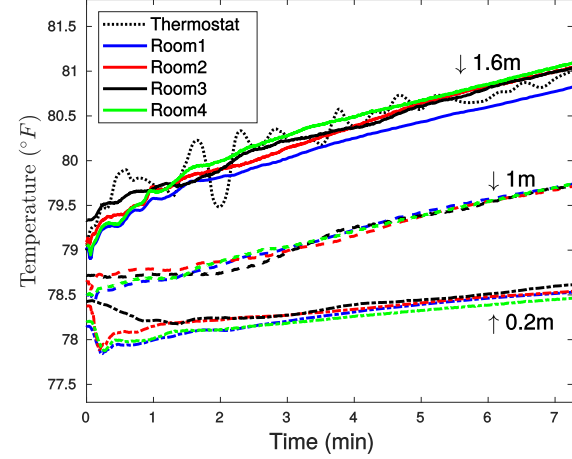
4.4. Interior temperature distribution

This section examines the details of the temperature distribution inside the house during the cooling and heating cycles, which can further explain the observed phenomena related to the cycle-to-cycle variability, overcooling, and the differences between the room temperatures. Fig. 19 shows the temperature distribution at the end of the cooling stage for the cycles 25 and 26 across a horizontal plane through $z = 1.6$ m, i.e., at the thermostat level. The figure shows a footprint of four cooling jets, two in the middle of both Rooms 1 and 2, and the other two in Room 4, which correspond to the cooling air descending from the air supply vents. The cooling air continues to descend until it hits the floor, upon which it starts coming up along the walls and the interior partitions of the rooms, as can be better viewed in Fig. 20 showing a vertical cross-section of the house passing through the $y = 2.1$ m line, i.e., through the center of the vents in the Rooms 1 and 4. The cooling air around the interior partitions between the inner rooms and Room 3 spills out into Room 3, and this is how the hallway is getting cooled, since it does not have its own air supply vent. Comparing Figs. 20 and 19(b), corresponding to the cycles 25 and 26, respectively, we see that the shorter cycle 25, terminated prematurely due to a cold plume impinging on a thermostat probe, leads to the overall higher temperatures inside the house, including Room 3 and the interior rooms; to the contrary, the longer cycle 26 results in significant overcooling of the whole space, and, especially, the interior rooms. Additionally, as seen before from the line plots, the hallway is typically warmer on average than the interior rooms at the thermostat level, supporting the argument that placing a single thermostat probe in a room that is not directly cooled results in the overcooling of the inner rooms.

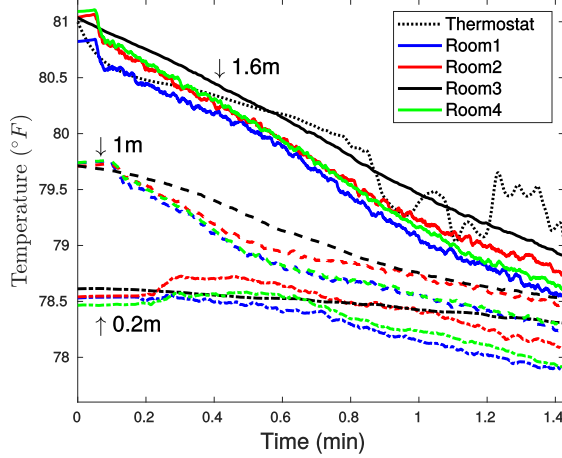
Figs. 21 and 22 show the temperature distribution at the end of the heating cycles 25 and 26 across the horizontal plane $z = 1.6$ m, and the vertical plane $y = 2.1$ m, respectively. As commented before, at the end of the heating cycle the air is much better mixed,



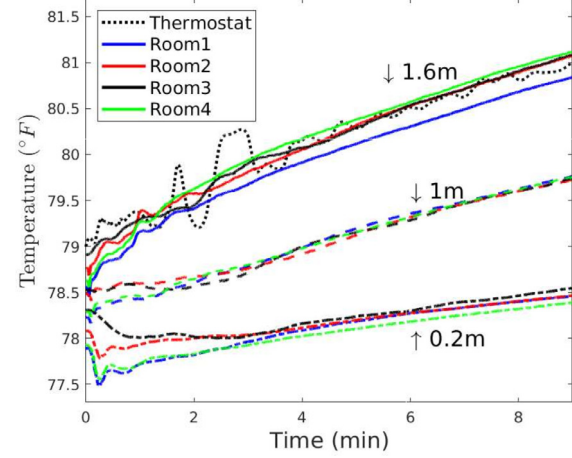
(a) Cycle 25: cooling.



(b) Cycle 25: heating.



(c) Cycle 26: cooling.



(d) Cycle 26: heating.

Fig. 16. Thermostat probe readings as compared to the room averaged temperatures at different heights. Black dotted line: thermostat reading; Blue lines: Room 1; Red lines: Room 2; Black lines: Room 3; Green lines: Room 4. Top plots (solid lines) are at a height of 1.6 m; middle plots (dashed lines), at a height of 1 m; bottom plots (dash-dotted lines), at a height of 0.2 m. (For interpretation of the references to color in this figure legend, the reader is referred to the web version of this article.)

the temperature distribution appears to be substantially more uniform, and the turbulent fluctuations are, overall, diminished, except near the walls and the windows, where thermal boundary layers result in a production of small-scale interacting cold and hot plumes. Note that such boundary layers do not form at the floor level, where adiabatic boundary conditions are set up, resulting in a zero mean temperature gradient, which can be seen in Fig. 22. From Figs. 16(b), 16(d), 17(b), 17(d), we observe that Room 1 is consistently colder by approximately 0.3 °F at the thermostat level at the end of the heating cycles, which seems to be a permanent feature of the flow, and not an attribute of a cycle variability. Indeed, the flow visualizations in Fig. 21 show that the temperature in Room 1 is lower for both the cycles 25 and 26 compared to the rest of the house. This can be explained by the fact that this is the only room in the house (apart from Room 3) that does not have windows. Indeed, Rooms 2 and 4 receive an additional heat through the windows. This strong thermal interaction between the cooled interior air and the hot window surfaces creates a very

interesting natural convection pattern shown in Fig. 23. It can be seen that the air, warming especially fast through the large windows in the living room, expands and pushes out of the living room, entering the colder Room 1 and creating a large recirculating vortex in Room 1. The effect of windows, although less significant, can be observed during the cooling cycles as well, resulting in the overall temperatures being the highest in Room 2 during cooling, followed by Room 4, and then Room 1, see Figs. 16(a), 16(c), 17(a), 17(c). In Room 4, we have a competing effect of larger window surfaces, but also stronger cooling coming from the two vents, which brings the temperature of Room 4 essentially down to the level of Room 1 during cooling, in spite of having windows.

5. Conclusions

The aim of the current study was to investigate the effects of an on/off operation of the air-conditioning system on the indoor air-

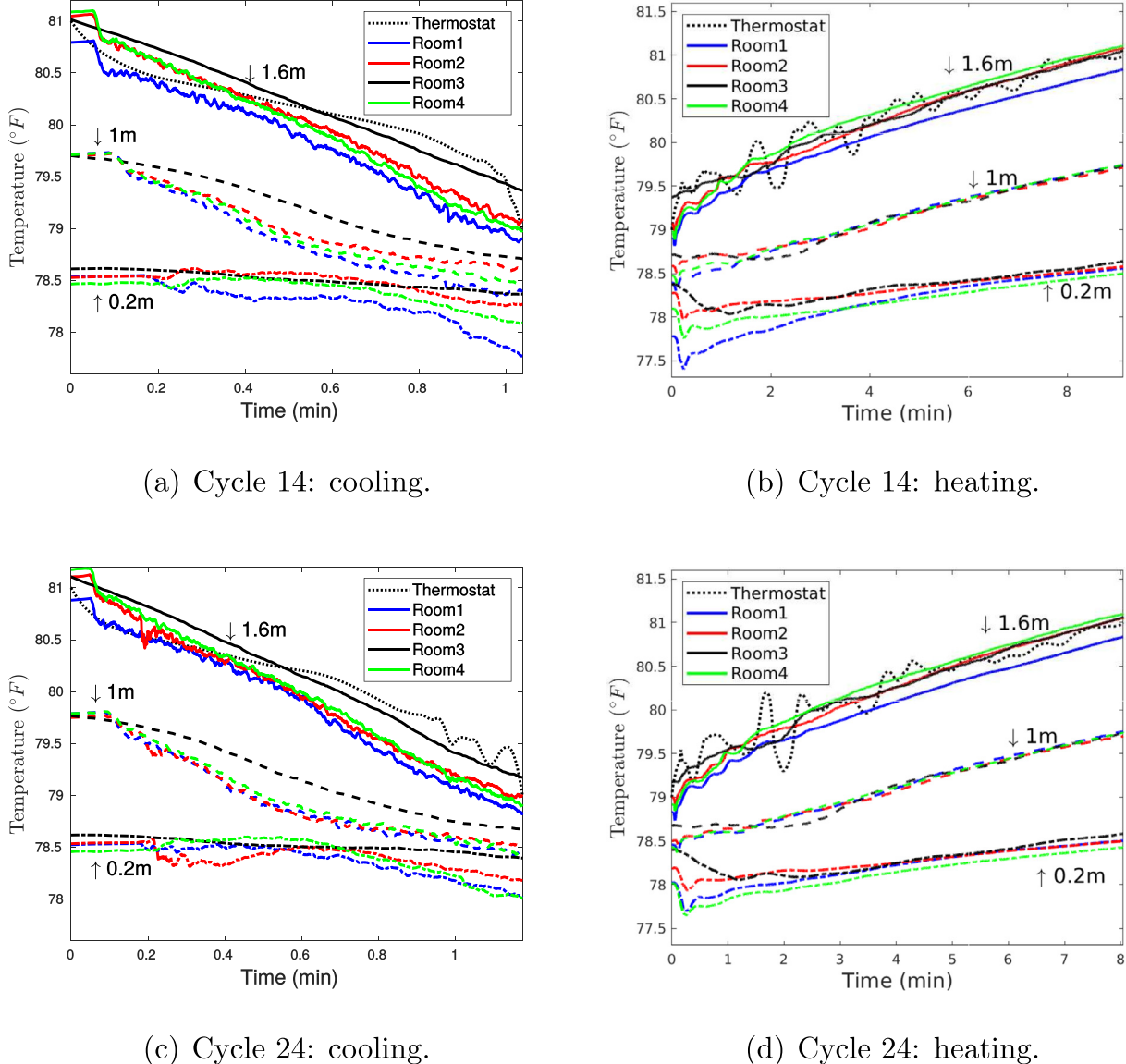
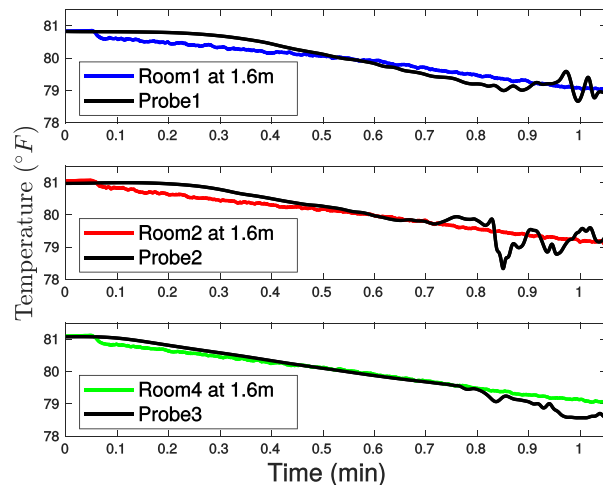


Fig. 17. Thermostat probe readings as compared to the room averaged temperatures at different heights for the AC cycles 14 and 24. Line labels are the same as in the caption to Fig. 16.

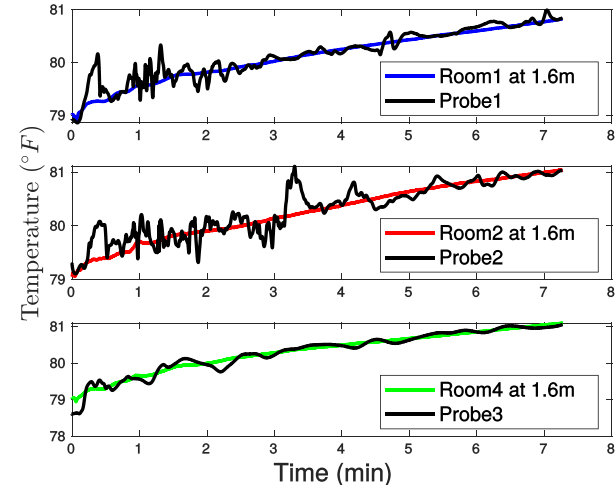
flow and temperature distribution within a medium-size single-floor residential house. For that, a Large Eddy Simulations methodology coupled with a conjugate heat transfer technique was developed and employed to simulate the initial heating and the subsequent 30 cooling and heating cycles within the model house, with the constant thermostat setpoint of 80 °F and a deadband of ± 1 °F. It was found that, even when the outdoor temperature and the thermostat setpoint temperature are held constant, the duration of the heating and cooling cycles does not stay the same, but varies significantly. The computed variability of 7–26% agrees well with the field data, which documents 7–22% variability [10], and with the EnergyPlus simulations [10]. As opposed to previous studies of the performance of air-conditioning systems with an on/off operation, either conducted using building energy simulations, or based on point-sensor measurements [10,12,13,17], the current work using LES allows not only to observe the cycle-to-cycle variability, but also to explain it from the perspectives of airflow dynamics. Specifically, it is concluded that the turbulent eddies associated with the mixing of cooling jets and a warm air can bring cold or hot parcels of gas in contact with the thermostat sensor,

which would either terminate the cooling cycle prematurely, or make it linger. This effect results in either overheating or overcooling of the space, and is not desirable. Additionally, it contributes to a power demand variability, and is disruptive for electric grid stability.

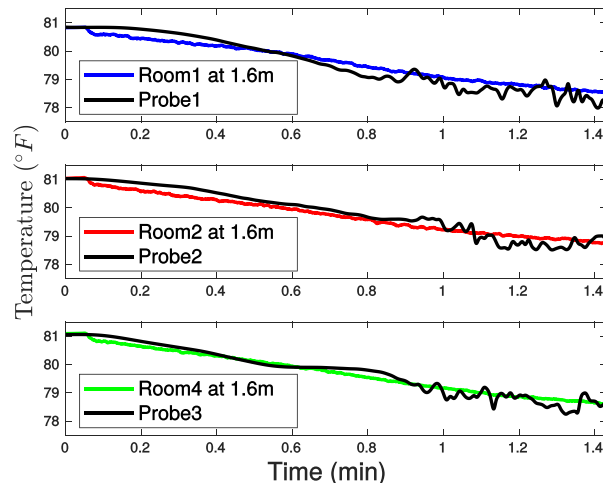
The current study also demonstrates a low effectiveness of a central thermostat control system. With a central thermostat system, the temperature in the entire house is largely controlled by a room where the thermostat is located. For example, in the current model house, the thermostat is in the hallway, which does not have its own cooling vent. When a hallway temperature reaches a set-point, the temperature in the other rooms, which have cooling vents, is significantly lower, which results in the overcooling of the house. The effect is even more exacerbated when the cooling cycle lasts longer than needed due to an appearance of a local hot spot (high temperature fluctuation) at the thermostat probe. As a consequence, in the current scenario, the house is almost always overcooled. The overcooling leads both to an excessive use of energy, and to a reduced thermal comfort. Note that, depending on the house layout, a central thermostat system could



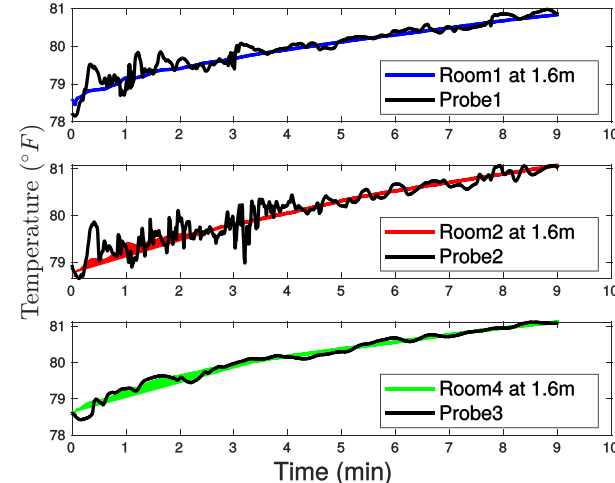
(a) Cycle 25: cooling.



(b) Cycle 25: heating.

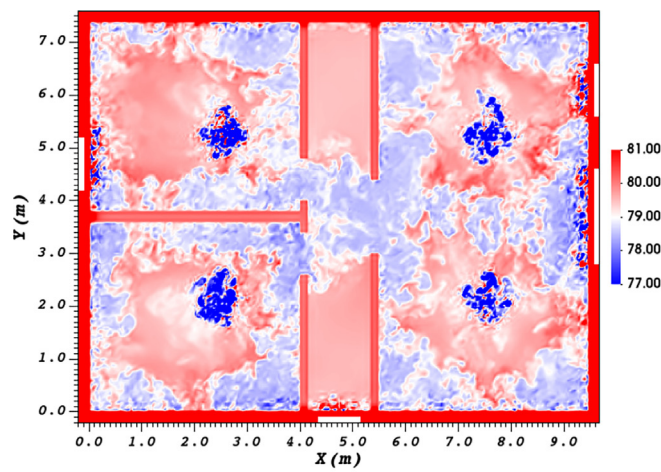


(c) Cycle 26: cooling.

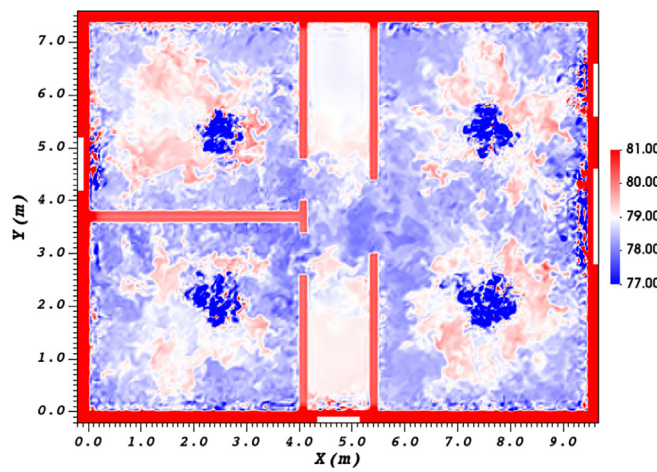


(d) Cycle 26: heating.

Fig. 18. Temperature at the remote sensor probes compared with the room averaged temperatures at a height of 1.6 m.

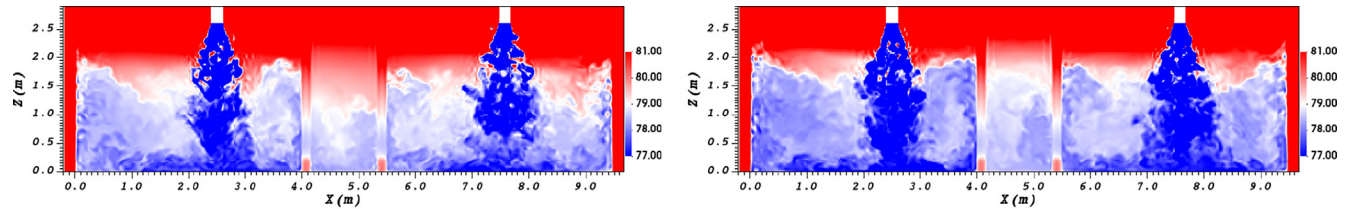


(a) Cycle 25.



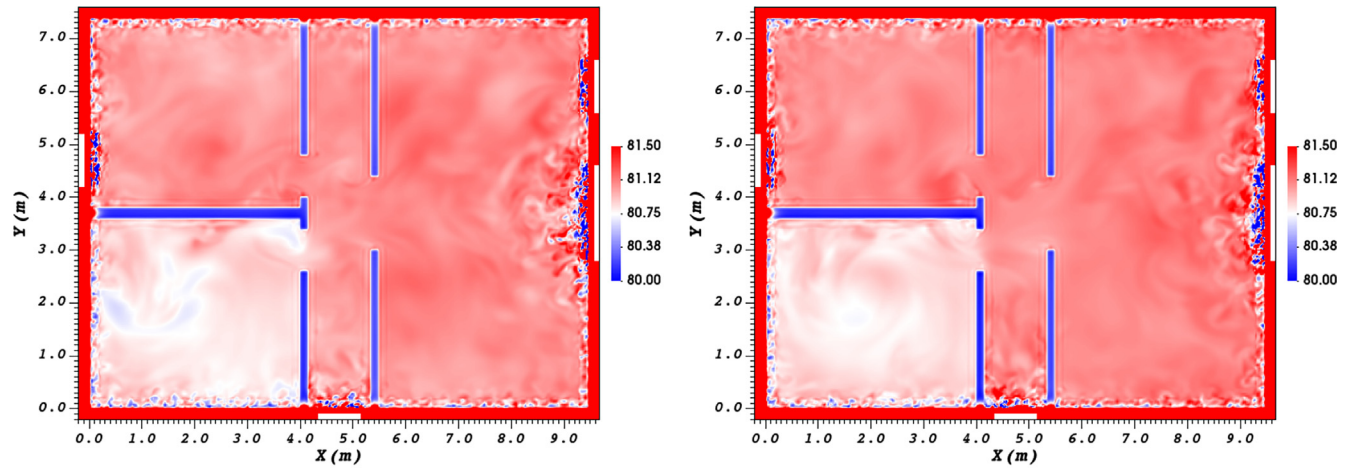
(b) Cycle 26.

Fig. 19. Temperature at the end of the cooling cycles 25 and 26, horizontal slice across the plane $z = 1.6\text{ m}$. Temperature is in $^{\circ}\text{F}$.



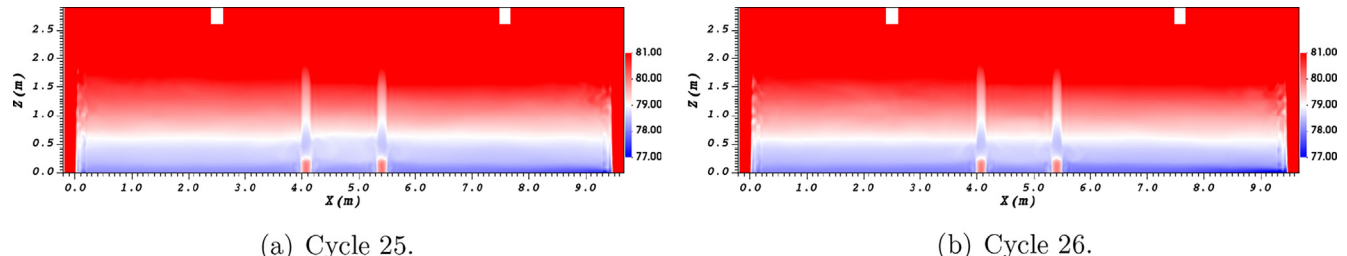
(a) Cycle 25.

(b) Cycle 26.

Fig. 20. Temperature at the end of the cooling cycles 25 and 26; vertical slice across the plane $y = 2.1$ m. Temperature is in $^{\circ}\text{F}$.

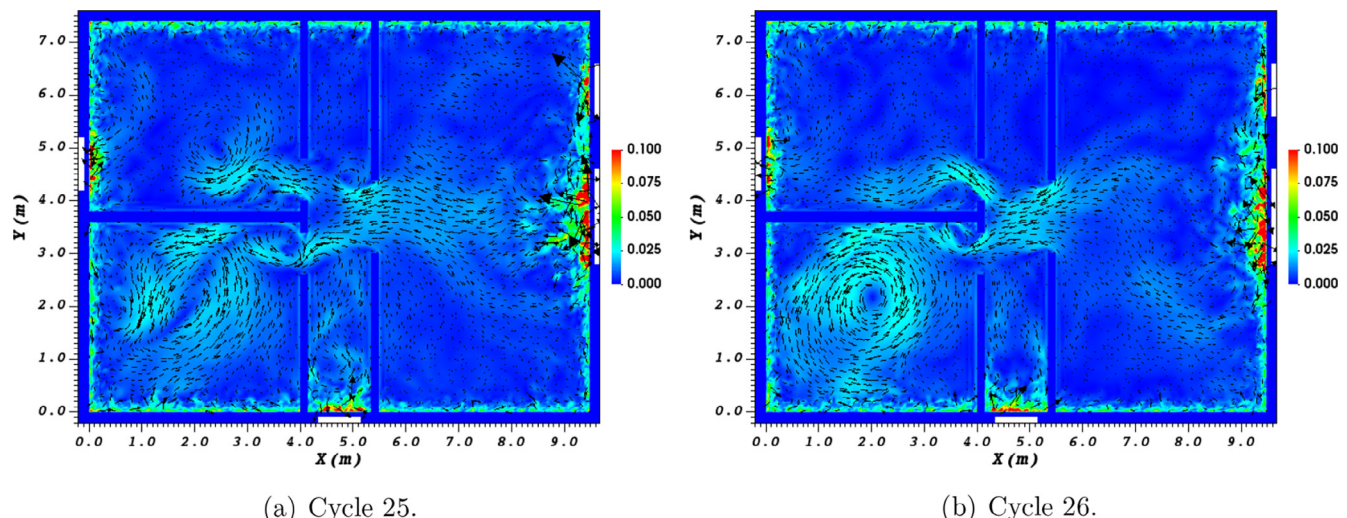
(a) Cycle 25.

(b) Cycle 26.

Fig. 21. Temperature at the end of the heating cycles 25 and 26; horizontal slice across the plane $z = 1.6$ m. Temperature is in $^{\circ}\text{F}$.

(a) Cycle 25.

(b) Cycle 26.

Fig. 22. Temperature at the end of the heating cycles 25 and 26; vertical slice across the plane $y = 2.1$ m. Temperature is in $^{\circ}\text{F}$.

(a) Cycle 25.

(b) Cycle 26.

Fig. 23. Velocity magnitude and in-plane velocity vectors at the end of the heating cycles 25 and 26; horizontal slice across the plane $z = 1.6$ m. Velocity is in m/s .

lead to a predominant overheating of the house, for example, if a thermostat is located close to a cooling vent.

Based on the current results, two remedies can be proposed to improve the effectiveness of an on/off air-conditioning system in a medium-size house. First, it is demonstrated that a zonal control system has a potential of being more successful in keeping the room temperatures close to a desired setpoint, since it was verified in the current LES that the remote sensor probes located within the rooms can track the average room temperatures consistently well. Second, to reduce a cycle-to-cycle variability, it can be recommended that the thermostat sensors not only consider instantaneous temperature readings, but also a time history of the signal, so that the turbulent fluctuations can be averaged out. For future work, it would be of interest to compare an on/off control strategy with other thermostat control strategies, such as, for example, PID or fuzzy control [5,6,12], and characterize their effect on the interior temperature distribution and cycle dynamics. Additionally, the effect of radiation should be considered in the future work. To the authors' knowledge, the presented work is the first study that addresses the effects of cyclic and an on/off AC equipment operation on the temperature distribution and the cycle variability, which influences thermal comfort, energy consumption, and power demand intermittency.

Declaration of Competing Interest

The authors declare that they have no known competing financial interests or personal relationships that could have appeared to influence the work reported in this paper.

Acknowledgements

The authors acknowledge the support of this work by a Joint Research Program between Arizona State University and Salt River Project power and water utility company in Tempe, AZ, with Aaron Dock and Patrick Malaty as the project managers. The simulations were performed on the Agave high-performance computing cluster supported by the ASU Research Computing initiative.

References

- [1] L. Pérez-Lombard, J. Ortiz, C. Pout, A review on buildings energy consumption information, *Energy Build.* 40 (2008) 1979–1988.
- [2] EIA, Use of energy explained: Energy use in homes, 2015, <https://www.eia.gov/energyexplained/use-of-energy/homes.php>.
- [3] Z.F. Tian, J.Y. Tu, G.H. Yeoh, R.K.K. Yuen, Numerical studies of indoor airflow and particle dispersion by large Eddy simulation, *Build. Environ.* 42 (2007) 3483–3492.
- [4] Q. Chen, Ventilation performance prediction for buildings: A method overview and recent applications, *Build. Environ.* 44 (2009) 848–858.
- [5] H. Mirinejad, S.H. Sadati, M. Ghasemian, H. Torab, Control techniques in heating, ventilating and air conditioning (HVAC) systems, *J. Comput. Sci.* 4 (2008) 777–783.
- [6] S. Wang, Z. Ma, Supervisory and optimal control of building HVAC systems: a review, *HVAC & R Res.* 14 (2008) 3–32.
- [7] A. Meier, C. Aragon, T. Peffer, D. Perry, M. Pritoni, Usability of residential thermostats: Preliminary investigations, *Build. Environ.* 46 (2011) 1891–1898.
- [8] D.W.U. Perera, C.F. Pfeiffer, N.-O. Skeie, Control of temperature and energy consumption in building - a review, *Int. J. Energy Envir.* 5 (2014) 471–484.
- [9] B. Li, G. Alleyne, Optimal on-off control of an air conditioning and refrigeration system, in: Proceedings of 2010 American Control Conference, Baltimore, MD, USA 978-1-4244-7427-1/10, 2010.
- [10] K.S. Cetin, M.H. Fathollahzadeh, N. Kunwar, H. Do, P.C. Tabares-Velasco, Development and validation of an HVAC on/off controller in EnergyPlus for energy simulation of residential and small commercial buildings, *Energy Build.* 183 (2019) 467–483.
- [11] W.H.J. Parken, R.W. Beausoliet, G.E. Kelly, Factors affecting the performance of a residential air-to-air heat pump, *ASHRAE Trans.* 83 (1977) 839–849.
- [12] G. Ulpiani, M. Borgognoni, A. Romagnoli, C. di Perna, Comparing the performance of on/off, PID and fuzzy controllers applied to the heating system of an energy-efficient building, *Energy Build.* 116 (2016) 1–17.
- [13] S.M. Ilic, C.W. Bullard, P.S. Hrnjak, Effect of shorter compressor on/off cycle times on A/C system performance, University of Illinois at Urbana-Champaign Tech. Report ACRC CR-43 (2001).
- [14] J.L. Gorter, HVAC equipment right-sizing: occupant comfort and energy-savings potential, *Energy Eng.* 109 (2012) 59–75.
- [15] J.P. Proctor, Field measurements of new residential air conditioners in phoenix, Arizona, *ASHRAE transactions* 103, In: Proceedings of ASHRAE Annual Meeting, Boston, MA, USA.
- [16] J.D. Rhodes, B. Stevens, M.E. Webber, Using energy audits to investigate the impacts of common air-conditioning design and installation issues on peak power demand and energy consumption in Austin, Texas, *Energy Build.* 43 (11) (2011) 3271–3278.
- [17] S.A. Tassou, C.J. Marquand, D. Wilson, Comparison of performance of capacity controlled and conventional on/off controlled heat pump, *Appl. Energy* 14 (1983) 241–256.
- [18] H. Henderson, D. Parker, Y. J. Huang, Improving DOE-2's RESYS routine: user defined functions to provide more accurate part load energy use and humidity prediction, In: Proceedings of 2000 ACEEE Summer Study on Energy Efficiency in Buildings, August 20–25, 2000 in Pacific Grove, CA LBNL-46304, 2000..
- [19] J. Winkler, J. Munk, J. Woods, Effect of occupant behavior and air-conditioner controls on humidity in typical and high-efficiency homes, *Energy Build.* 165 (2018) 364–378.
- [20] K.S. Cetin, Characterizing large residential appliance peak load reduction potential utilizing a probabilistic approach, *Sci. Technol. Built Environ.* 22 (2016) 720–732.
- [21] E.B.T. Tchuisseu, D. Gomila, D. Brunner, P. Colet, Effects of dynamic-demand-control appliances on the power grid frequency, *Phys. Rev. E* 96 (2017) 1979–1988.
- [22] J. Park, T. Kim, C.-S. Lee, Development of thermal comfort-based controller and potential reduction of the cooling energy consumption of a residential building in Kuwait, *Energies* 12 (17) (2019) 3348.
- [23] H.I. Henderson, D.B. Shirey, R.A. Rastad, Closing the gap: getting full performance from residential central air conditioners, Task 4 – Develop new climate-sensitive air-conditioner, simulation results and cost benefit analysis, New York State Energy Research and Development Authority, 2007..
- [24] C. Booten, C. Christensen, J. Winkler, Energy impacts of oversized residential air-conditioners - Simulation study of retrofit sequence impacts, National Renewable Energy Laboratory NREL/TP-5500-60801 (2014).
- [25] T. Tran-Quoc, J.C. Sabonnadière, Air conditioner direct load control in distribution networks, In: Proceedings of 2009 IEEE Bucharest Power Tech Conference, Bucharest, Romania, 2009..
- [26] M. Hummon, D. Palchak, P. Denholm, J. Jorgenson, D. J. Olsen, S. Kiliccote, N. Matson, M. Sohn, C. Rose, J. Dudley, S. Goli, O. Ma, Grid integration of aggregated demand response, Part 2: Modeling demand response in a production cost model, Tech. Rep. NREL/TP-6A20-58492, 2013..
- [27] M. M. Ameen, M. Mirzaeiyan, F. Millo, S. Som, Numerical prediction of cyclic variability in a spark ignition engine using a parallel large eddy simulation approach, *J. Energy Res. Technol.* 140 (5)..
- [28] O. Benoit, K. Truffin, S. Jay, J. van Oijen, Y. Drouvin, T. Kayashima, P. Adomeit, C. Angelberger, Development of a large-eddy simulation methodology for the analysis of cycle-to-cycle combustion variability of a lean burn engine, *Flow Turbul. Combust.* (2021) 1–40.
- [29] C. Buratti, D. Palladino, E. Moretti, Prediction of indoor conditions and thermal comfort using CFD simulations: a case study based on experimental data, *Energy Procedia* 126 (2017) 115–122.
- [30] G. Semprini, A. Jahanbin, B. Pulvirenti, P. Guidorzi, Evaluation of thermal comfort inside an office equipped with a fan coil HVAC system: A CFD approach, *Future Cities Environ.* 5 (1)..
- [31] G.A. Ganesh, S.L. Sinha, T.N. Verma, Numerical simulation for optimization of the indoor environment of an occupied office building using double-panel and ventilation radiator, *J. Build. Eng.* 29 (2020) 101139.
- [32] X. Shan, W. Xu, Y.-K. Lee, W.-Z. Lu, Evaluation of thermal environment by coupling CFD analysis and wireless-sensor measurements of a full-scale room with cooling system, *Sustain. Cities Soc.* 45 (2019) 395–405.
- [33] Z. Chen, J. Xin, P. Liu, Air quality and thermal comfort analysis of kitchen environment with CFD simulation and experimental calibration, *Build. Environ.* 172 (2020) 106691.
- [34] A. Jahanbin, G. Semprini, Numerical study on indoor environmental quality in a room equipped with a combined hrv and radiator system, *Sustainability* 12 (24) (2020) 10576.
- [35] S.A. Nada, H.M. El-Batsh, H.F. Elattar, N.M. Ali, CFD investigation of airflow pattern, temperature distribution and thermal comfort of UFAD system for theater buildings applications, *J. Build. Eng.* 6 (2016) 274–300.
- [36] Z.J. Zhai, Q.Y. Chen, Performance of coupled building energy and CFD simulations, *Energy Build.* 37 (2005) 333–344.
- [37] H. Chen, Z. Feng, S.-J. Cao, Quantitative investigations on setting parameters of air conditioning (air-supply speed and temperature) in ventilated cooling rooms, *Indoor Built Environ.* (2019) 1420326X19887776.
- [38] J. Clarke, W. Dempster, C. Negrao, The implementation of a computational fluid dynamics algorithm within the ESP-r system, *Proc. Build. Simul.* (1995) 166–175.
- [39] P.V. Nielsen, T. Trytvason, Computational fluid dynamics and building energy performance simulation, proceedings of Roomvent, vol. 1, Stockholm, Sweden, 1998, pp. 101–107.

- [40] Z. Zhai, Q. Chen, P. Haves, J.H. Klems, On approaches to couple energy simulation and computational fluid dynamics programs, *Build. Environ.* 37 (2002) 857–864.
- [41] B. Pandey, R. Banerjee, A. Sharma, Coupled EnergyPlus and CFD analysis of PCM for thermal management of buildings, *Energy Build.* 231 (2021) 110598.
- [42] D. Kaminski, C. Prakash, Conjugate natural convection in a square enclosure: effect of conduction in one of the vertical walls, *Int. J. Heat Mass Transfer* 29 (1986) 1979–1988.
- [43] A. Muftuoglu, E. Bilgen, Conjugate heat transfer in open cavities with a discrete heater at its optimized position, *Int. J. Heat Mass Transfer* 51 (2008) 779–788.
- [44] G.V. Kuznetsov, M.A. Sheremet, Conjugate natural convection in an enclosure with a heat source of constant heat transfer rate, *Int. J. Heat Mass Transfer* 54 (2011) 260–268.
- [45] K. Horikiri, Y. Yao, J. Yao, Modelling conjugate flow and heat transfer in a ventilated room for indoor thermal comfort assessment, *Build. Environ.* 77 (2014) 135–147.
- [46] M. Embaye, R. Al-Dadah, S. Mahmoud, Numerical evaluation of indoor thermal comfort and energy saving by operating the heating panel radiator at different flow strategies, *Energy Build.* 121 (2016) 298–308.
- [47] M.A. Antar, H. Baig, Conjugate conduction–natural convection heat transfer in a hollow building block, *Appl. Therm. Eng.* 29 (17–18) (2009) 3716–3720.
- [48] E. Troppová, J. Tippner, M. Švehlík, Numerical and experimental study of conjugate heat transfer in a horizontal air cavity, in: *Building Simulation*, vol. 11, Springer, 339–346, 2018.
- [49] C. Sinn, G.R. Pesch, J. Thöming, L. Kiewidt, Coupled conjugate heat transfer and heat production in open-cell ceramic foams investigated using CFD, *Int. J. Heat Mass Transfer* 139 (2019) 600–612.
- [50] D. Xie, Y. Wang, H. Wang, S. Mo, M. Liao, Numerical analysis of temperature non-uniformity and cooling capacity for capillary ceiling radiant cooling panel, *Renew. Energy* 87 (2016) 1154–1161.
- [51] A. Radwan, T. Katsura, L. Ding, A. A. Serageldin, A. I. EL-Seesy, K. Nagano, Design and thermal analysis of a new multi-segmented mini channel based radiant ceiling cooling panel, *J. Build. Eng.* 40 (2021) 102330.
- [52] A. Tariq, K. Altaf, S.W. Ahmad, G. Hussain, T.A. Ratlamwala, Comparative numerical and experimental analysis of thermal and hydraulic performance of improved plate fin heat sinks, *Appl. Therm. Eng.* 182 (2021) 115949.
- [53] H. Xiao, Z. Liu, W. Liu, Conjugate heat transfer enhancement in the mini-channel heat sink by realizing the optimized flow pattern, *Appl. Therm. Eng.* 182 (2021) 116131.
- [54] P. Fischer, J. Lottes, S. Kerkmeyer, O. Marin, K. Heisey, A. Obabko, E. Merzari, Y. Peet, Nek5000:User's manual, Technical Report ANL/MCS-TM-351, Argonne National Laboratory, <http://nek5000.mcs.anl.gov>, 2015.
- [55] Y. Peet, P. F. Fischer, Heat transfer LES simulations in application to wire-wrapped fuel pins, AIAA Paper 2010-4318, in: 10th AIAA/ASME Joint Thermophysics and Heat Transfer Conference, June 28–July 1 2010, Chicago, IL, 2010.
- [56] T. Chatterjee, Y.T. Peet, Regularization modelling for large-eddy simulation in wall-bounded turbulence: An explicit filtering-based approach, *Int. J. Numer. Meth. Fluids* 88 (1) (2018) 1–17.
- [57] A.T. Patera, A spectral element method for fluid dynamics: Laminar flow in a channel expansion, *J. Comp. Phys.* 54 (3) (1984) 468–488.
- [58] M.O. Deville, P.F. Fischer, E.H. Mund, *High-Order Methods for Incompressible Fluid Flow*, Cambridge University Press, 2002.
- [59] P.J. Sakievich, Y.T. Peet, R.J. Adrian, Large-scale thermal motions of turbulent rayleigh–bénard convection in a wide aspect-ratio cylindrical domain, *Int. J. Heat Fluid Flow* 1–14 (2016).
- [60] P.F. Fischer, An overlapping Schwarz method for spectral element solution of the incompressible Navier-Stokes equations, *J. Comp. Phys.* 133 (1) (1997) 84–101.
- [61] E. Merzari, A. Obabko, P. F. Fischer, Spectral element methods for liquid metal reactors applications, von Karman Institute for Fluid Dynamics, in *Thermohydraulics and Chemistry of Liquid Metal Cooled Reactors*, Edited by F. Roelofs & Ph. Planquart, VKI LS 2017-02, 2017..
- [62] P.F. Fischer, J. Mullen, Filter-based stabilization of spectral element methods, *Comptes Rendus de l'Académie des sciences, Série I- Analyse numérique* 332 (2001) 265–270.
- [63] J.-L. Guermond, S. Prudhomme, Mathematical analysis of a spectral hyperviscosity LES model for the simulation of turbulent flows, *Math. Model. Numer. Anal.* 37 (2003) 893–908.
- [64] L.C. Berselli, T. Iliescu, W.J. Layton, *Mathematics of Large Eddy Simulation of Turbulent Flows*, Springer Verlag, Berlin, 2006.
- [65] B. Geurts, A.K. Kuczaj, E.S. Titi, Regularization modelling for large-eddy simulation of homogeneous isotropic decaying turbulence, *J. Phys. A: Math. Theor.* 41 (2008) 344008.
- [66] G.S. Karamanos, G.E. Karniadakis, A spectral vanishing viscosity method for large eddy simulations, *J. Comput. Phys.* 163 (2000) 22–50.
- [67] M. Visbal, P. Morgan, D. Rizzetta, An implicit LES approach based on high-order compact differencing and filtering schemes, in: 16th AIAA Computational Fluid Dynamics Conference, 4098, 2003..
- [68] B.J. Geurts, Regularization modeling for LES of separated boundary layer flow, *J. Fluids Struct.* 24 (2008) 1176–1184.
- [69] P. Fischer, J. Lottes, D. Pointer, A. Siegel, Petascale algorithms for reactor hydrodynamics, *J. Phys. Conf. Series* 125 (2008) 012076.
- [70] Y. Peet, P. Fischer, G. Conzelmann, V. Kotamarthi, Actuator line aerodynamics model with spectral elements, AIAA Paper 2013-1210, 51st Aerospace Sciences Meeting, Grapevine, TX, 2013.
- [71] A.V. Obabko, P.F. Fischer, T.J. Tautges, V.M. Goloviznin, M.A. Zaytsev, V.V. Chudanov, V.A. Pervichko, A.E. Aksanova, S. Karabasov, Large Eddy Simulation of thermo-hydraulic mixing in a T-Junction, in: Nuclear Reactor Thermal Hydraulics and Other Applications, Donna Post Guillen, Ed., ISBN 978-953-51-0987-7, 2013..
- [72] J.D. Posner, C.R. Buchanan, D. Dunn-Rankin, Measurement and prediction of indoor air flow in a model room, *Energy Build.* 35 (2003) 515–526.
- [73] H. Wang, Z.J. Zhai, Advances in building simulation and computational techniques: A review between 1987 and 2014, *Energy Build.* 128 (2016) 319–335.
- [74] J. Liu, S. Zhu, M.K. Kim, J. Srebric, A review of CFD analysis methods for personalized ventilation (PV) in indoor built environments, *Sustainability* 11 (15) (2019) 4166.
- [75] S. Pandey, Y.G. Park, M.Y. Ha, An exhaustive review of studies on natural convection in enclosures with and without internal bodies of various shapes, *Int. J. Heat Mass Transfer* 138 (2019) 762–795.
- [76] P.J. Sakievich, Y.T. Peet, R.J. Adrian, Temporal dynamics of large-scale structures for turbulent Rayleigh–Bénard convection in a moderate aspect-ratio cylinder, *J. Fluid Mech.* 901..
- [77] N. G. Ivanov, M. A. Zasimova, Large Eddy Simulation of airflow in a test ventilated room, in: *Journal of Physics: Conference Series*, vol. 1038, IOP Publishing, 012136, 2018..
- [78] F. Xu, S. Xu, U. Pasie, B. Ganapathysubramanian, Computational study of natural ventilation in a sustainable building with complex geometry, *Sustain. Energy Technol. Assess.* 45 (2021) 101153.
- [79] C. Li, Y. Zhao, Y. He, K.H. Luo, Y. Li, Simulation of indoor harmful gas dispersion and airflow using three-dimensional lattice Boltzmann method based large-eddy simulation, *AIP Adv.* 11 (3) (2021) 035235.
- [80] C. Hirose, N. Ikegaya, A. Hagishima, J. Tanimoto, Indoor airflow and thermal comfort in a cross-ventilated building within an urban-like block array using large-eddy simulations, *Build. Environ.* 196 (2021) 107811.
- [81] J.D. Chung, H. Hong, H. Yoo, Analysis on the impact of mean radiant temperature for the thermal comfort of underfloor air distribution systems, *Energy Build.* 42 (12) (2010) 2353–2359.
- [82] R.G. dos Santos, M. Lecanu, S. Ducruix, O. Gicquel, E. Iacona, D. Veynante, Coupled large eddy simulations of turbulent combustion and radiative heat transfer, *Combust. Flame* 152 (3) (2008) 387–400.
- [83] K. Yamamoto, T. Murota, T. Okazaki, K. Ouryouji, Parallel radiative heat transfer calculation method for large eddy simulation on unstructured mesh, *Trans. Japan Soc. Mech. Eng. Part B* 75 (9) (2009) 2299–2307.
- [84] C. Fureby, Large eddy simulation of turbulent reacting flows with conjugate heat transfer and radiative heat transfer, *Proc. Combust. Inst.* 38 (2) (2021) 3021–3029.
- [85] S. Mittal, On the performance of high aspect ratio elements for incompressible flows, *Comput. Methods Appl. Mech. Eng.* 188 (1–3) (2000) 269–287.
- [86] R. Courant, K. Friedrichs, H. Lewy, On the partial difference equations of mathematical physics, *IBM J. Res. Dev.* 11 (2) (1967) 215–234.
- [87] B.M. Svoma, A. Brazel, Urban effects on the diurnal temperature cycle in Phoenix, Arizona, *Clim. Res.* 41 (1) (2010) 21–29.
- [88] M. Tewari, F. Salamanca, A. Martilli, L. Treinish, A. Mahalov, Impacts of projected urban expansion and global warming on cooling energy demand over a semiarid region, *Atmos. Sci. Lett.* 18 (11) (2017) 419–426.
- [89] Q. Chen, J. Srebric, A procedure for verification, validation, and reporting of indoor environment CFD analyses, *Hvac&R Res.* 8 (2) (2002) 201–216.
- [90] Z. Ai, C.M. Mak, Potential use of reduced-scale models in CFD simulations to save numerical resources: Theoretical analysis and case study of flow around an isolated building, *J. Wind Eng. Ind. Aerodyn.* 134 (2014) 25–29.
- [91] G. Zoll, CFD Analysis with scale model verification – a proven cost-effective approach, in: *Power Engineering*, 2019..
- [92] B. Sparn, K. Hudon, L. Earle, C. Booten, P. Tabares-Velasco, G. Barker, C. Hancock, Greenbuilt retrofit test house final report, Tech. Rep., National Renewable Energy Lab.(NREL), Golden, CO (United States), 2014..
- [93] M.C. Baechler, J. Williamson, T. Gilbride, P. Cole, M. Hefty, P. Love, Guide to determining climate regions by county, Pacific Northwest National Laboratory & Oak Ridge National Laboratory 7 (2010) 1–34.
- [94] J.H. Whitelaw, Convective heat transfer, in: *Thermopedia: Heat & Mass Transfer, and Fluids Engineering*, URL: 2011, DOI: 10.1615/AtoZ.c.convective_heat_transfer..
- [95] P. Kosky, R. Balmer, W. Keat, G. Wise, *Exploring Engineering*, 5th Edition, Academic Press, Elsevier Inc., 2021.